Monthly Notices of the ROYAL ASTRONOMICAL SOCIETY

MNRAS **548,** 1–25 (2026) https://doi.org/10.1093/mnras/stag808
Advance Access publication 2026 April 30

Hitting the slopes: a spectroscopic view of UV continuum slopes of galaxies reveals a reddening at $z > 9.5$

Aayush Saxena [1,2★] Alex J. Cameron [1] Harley Katz,[3,4] Andrew J. Bunker [1] Jacopo Chevallard,[1] Francesco D'Eugenio,[5,6] Santiago Arribas,[7] Rachana Bhatawdekar,[8] Kristan Boyett [1] Phillip A. Cargile,[9] Stefano Carniani [10] Stéphane Charlot [11] Mirko Curti [12] Emma Curtis-Lake [13] Kevin Hainline,[14] Zhiyuan Ji,[14] Benjamin D. Johnson,[9] Gareth C. Jones [5,6] Nimisha Kumari [15] Isaac Laseter,[16] Michael V. Maseda [16] Brant Robertson,[17] Charlotte Simmonds,[5,6] Sandro Tacchella [5,6] Hannah Übler [18] Christina C. Williams,[19] Chris Willott,[20] Joris Witstok [21,22] and Yongda Zhu [14]

Affiliations are listed at the end of the paper

Accepted 2026 April 24. Received 2026 April 24; in original form 2024 November 26

ABSTRACT

The ultraviolet (UV) continuum slope of galaxies, β, is a powerful diagnostic of the metallicity and ages of stars, nebular gas properties, dust content, and the escape of Lyman continuum (LyC) photons. In this study, we present β measurements for 395 spectroscopically confirmed galaxies at $5 < z < 14.3$ selected primarily from JADES, using high-quality *JWST* (*James Webb Space Telescope*) NIRSpec/PRISM spectra. We find a median $\beta = -2.15$, finding a mild increase in blueness of β with increasing redshift and fainter UV magnitudes. Interestingly, we find evidence for reddening of the average β at $z > 9.5$, deviating from the trend observed at $z < 9.5$. Using stacked spectra in bins of redshift and β, we derive trends between β and dust attenuation, metallicity, ionization parameter, and stellar age indicators, finding a lack of dust attenuation to be the dominant driver of bluer β-values. We further report five galaxies with $\beta \leq -2.9$, which show a range of spectroscopic properties and signs of significant LyC photon leakage. Finally, we show that the redder β-values at $z > 9.5$ may require rapid build-up of dust reservoirs in the very early Universe or a significant contribution from the nebular continuum emission to the observed UV spectra, with the nebular continuum fraction depending on the gas temperatures and densities. We show that in the absence of dust, nebular emission at $n_e > 10\,000\,\mathrm{cm}^{-3}$ can reproduce the range of red β that we see in our sample. Higher gas densities can also redden the nebular continuum emission, potentially explaining the observed β-values.

Key words: galaxies: evolution – galaxies: high-redshift – galaxies: ISM – galaxies: star formation.

1 INTRODUCTION

The rest-frame ultraviolet (UV) continuum slope of galaxy spectra, β, which is parametrized as $f_\lambda \propto \lambda^\beta$, is an important quantity that can be used as a diagnostic of the nature of stellar populations and physical and chemical properties of the nebular gas in galaxies, the age and metallicity of stars, and the dust content (D. Calzetti, A. L. Kinney & T. Storchi-Bergmann 1994). Detailed insights about the evolution of β as a function of redshift can be used to infer the metallicity evolution (e.g. A. Calabrò et al. 2021), the change in the dust content in star-forming galaxies (e.g. R. J. Bouwens et al. 2009; S. M. Wilkins et al. 2013) and potentially the escape fraction of Lyman continuum (LyC) photons, that is crucial for evaluating the contribution of galaxies to the cosmic reionization budget (e.g. J. Chisholm et al. 2022).

Before the launch of *James Webb Space Telescope* (*JWST*), pioneering work has been done in measuring the evolution of β with redshift for statistically significant samples of galaxies into the epoch of reionization using deep *Hubble Space Telescope* (*HST*) imaging (e.g. R. J. McLure et al. 2011; J. S. Dunlop et al. 2012; S. L. Finkelstein et al. 2012; S. M. Wilkins et al. 2013; R. J. Bouwens et al. 2014; R. Bhatawdekar & C. J. Conselice 2021; S. Tacchella et al. 2022). One of the main aims of such studies has been to identify galaxies with extremely blue UV slopes ($\beta \lesssim -3.0$) at $z > 6$, which would likely trace extremely metal-poor and dust-free galaxies that are also possibly leaking a significant fraction of LyC photons to drive reionization (e.g. A. Bolamperti et al. 2023). Indeed, some evidence of the existence of such blue UV slopes was reported (e.g. R. J. Bouwens et al. 2010; S. L. Finkelstein et al. 2010). However, subsequent studies showed that these very blue

★ E-mail: aayush.saxena@physics.ox.ac.uk

β measurements may suffer from observational and sample selection biases and that the median UV slope of $z \sim 7$ galaxies may be nearer to $\beta \sim -2.5$ (e.g. J. S. Dunlop et al. 2012; S. L. Finkelstein et al. 2012; R. Bhatawdekar & C. J. Conselice 2021). Further theoretical studies have also shown that at extremely low metallicities, the fraction of the total UV continuum at 1500 Å dominated by the nebular continuum components increases, thereby reddening the β-value (e.g. A. Raiter, D. Schaerer & R. A. E. Fosbury 2010; A. J. Cameron et al. 2023a; H. Katz et al. 2024).

With *JWST*, it is now finally possible to push measurements of β for statistical samples of galaxies out to $z > 10$. There have already been a number of studies exploring the dependence of β both on redshift as well as the absolute UV magnitudes ($M_{\rm UV}$) using deep Near Infrared Camera (NIRCam) imaging data out to $z > 9$ (e.g. M. W. Topping et al. 2022, 2024; R. J. Bouwens et al. 2023; L. J. Furtak et al. 2023; T. Nanayakkara et al. 2023; F. Cullen et al. 2023a, b; D. Austin et al. 2024). Interestingly, most of these studies find evidence for the existence of galaxies with very blue UV slopes ($\beta < -2.7$), with a trend showing that UV-fainter galaxies consistently having bluer β-values.

Although studies relying on photometric data alone can lead to the identification of large samples, and can inherently be more 'complete' in terms of the UV magnitude selection, they have their limitations. Perhaps the biggest source of uncertainty in photometrically driven studies is the accuracy of photometric redshifts, and therefore the purity of the sample selection, particularly at fainter UV magnitudes (e.g. R. Bouwens et al. 2023). Contamination from strong rest-frame UV emission lines can also affect the measured β from broad-band photometry alone, particularly if strong Lyα emission is present in one of the crucial bands used to infer β. Finally, based on photometry alone, there is an unavoidable need to employ spectral energy distribution (SED) modelling to both accurately measure β over the appropriate wavelength range as well as infer the physical and chemical properties of galaxies, which is crucial for breaking degeneracies between various parameters (such as dust reddening, age and metallicity of the stellar populations, etc.), which are responsible for setting the various features seen in the rest-frame UV spectra (e.g. F. Cullen et al. 2023b; M. W. Topping et al. 2024).

Thanks to large spectroscopic programs also being carried out by *JWST*, particularly using the lower resolution PRISM/CLEAR configuration of the Near Infrared Spectrograph (NIRSpec) instrument (P. Ferruit et al. 2022; P. Jakobsen et al. 2022), which gives simultaneous coverage across observed wavelengths of $\sim 0.6 - 5.3$ μm, it is now possible to spectroscopically measure the rest-frame UV continuum slopes of a large number of galaxies at high redshifts (e.g. M. J. Hayes et al. 2024; K. E. Heintz et al. 2024; G. Roberts-Borsani et al. 2024). These studies have already shown a steady increase in the blueness of β with redshifts across a range of UV magnitudes, which have been interpreted as the systematic reduction in the dust content of galaxies at earlier epochs, in line with findings from photometric studies. Additionally, β measurements for some of the highest redshift galaxies, such as $\beta = -2.3$ for JADES-GS-z14-0 at $z = 14.32$ (S. Carniani et al. 2024), $\beta = -2.5$ for GHZ2 at $z = 12.34$ (M. Castellano et al. 2024) and $\beta = -2.4$ for GN-z11 at $z = 10.6$ (A. J. Bunker et al. 2023b) now offer a remarkable opportunity to study the stellar and gas conditions within these record-breaking galaxies that regulate the emerging UV continuum slopes.

A key advantage of using spectroscopy to infer β is the ability to mask UV metal lines, and the availability of a plethora of other key diagnostics available in galaxy spectra that can further shed light on the underlying physical and chemical conditions in the galaxies that may be responsible for setting the UV continuum slope (e.g. A. Calabrò et al. 2021). As mentioned earlier, key galaxy properties such as the age and metallicity of stars and gas, as well as the gas temperatures and densities can be inferred reliably from spectra using diagnostics relying on emission-line fluxes and ratios, which play an important role in setting the UV slope of galaxies. To therefore understand the physical conditions within galaxies that may give rise to any relationship between β and redshift or UV magnitude, performing an analysis on spectroscopically confirmed galaxies with robust detection of the UV continuum and emission lines is key.

In this study, we use a sample of 295 spectroscopically confirmed galaxies at $z > 5.5$, spanning a wide range of UV magnitudes, to investigate the observed β in galaxies at the highest redshifts. A key aim is to study how the redshift evolution of these properties could be used to explain the observed evolution in the UV continuum slopes of galaxies deep in the reionization era. We perform UV continuum slope measurements both for individual galaxy spectra as well as on stacked spectra constructed in carefully chosen bins in an attempt to inform both the median evolution of β, as well as what drives the scatter in its value over cosmic time, leveraging a number of diagnostics from galaxy spectra.

The layout of this paper is as follows. In Section 2, we describe the spectroscopic data sets and present the methodology used to perform measurements of quantities from galaxy spectra, including the β using a novel Monte Carlo method. In Section 3, we present the main findings of our analysis, exploring the redshift evolution of β, its dependence on $M_{\rm UV}$, its correlation with galaxy physical and chemical properties using both individual measurements and stacking, as well as the discovery of a sample of galaxies showing $\beta \lesssim -3.0$. In Section 4, we focus on β measured for galaxies at $z > 9.5$, highlighting the relatively redder β measurements and its implications on the nature of some of the first galaxies that formed in the Universe. In Section 5, we summarize the key findings of this study.

Throughout this paper, we use the Planck Collaboration VI (2020) cosmology. Magnitudes are in the AB system (J. B. Oke & J. E. Gunn 1983) and all distances used are proper distances, unless otherwise stated. We adopt a solar metallicity of $Z_\odot = 0.02$.

2 DATA AND MEASUREMENTS

2.1 JADES spectroscopic data

The data sets used in this work come from the *JWST* Advanced Deep Extragalactic Survey (JADES; D. J. Eisenstein et al. 2023a; A. J. Bunker, NIRSPEC Instrument Science Team & JAESs Collaboration 2020), which has leveraged NIRSpec and NIRCam guaranteed time observations to obtain some of the deepest spectra and imaging of galaxies at high redshifts in the well-studied Great Observatories Origins Deep Surveys (GOODS)-South and North fields. The survey was designed such that 'medium' depth observations were obtained across both fields, with two additional 'deep' tier pointings observed in the GOODS-South field containing the footprint of the Hubble Ultra Deep Field (HUDF; A. J. Bunker et al. 2023a). NIRSpec observations as part of JADES were obtained over a period of around 18 months, starting in 2022 October and ending in 2024 February. Complementary NIRCam

images in the fields were also obtained as part of JADES (M. J. Rieke et al. 2023). For a full overview of JADES observations, survey design, coverage area, overlap with archival and other *JWST* data, and survey depth and sensitivity, we refer the readers to D. J. Eisenstein et al. (2023a) and F. D'Eugenio et al. (2024).

The NIRSpec observations in both fields across all tiers were carried out in multi-object spectroscopy mode (P. Ferruit et al. 2022) in four filter/disperser combinations. These were the lowest resolution ($R \sim 30 - 300$) but highest sensitivity PRISM/CLEAR configuration covering the full-wavelength range from $\approx 0.6 - 5.3\,\mu$m, along with three intermediate spectral resolution observations in *G*140*M*/*F*070*LP*, *G*235*M*/*F*170*LP*, and *G*395*M*/*F*290*LP* giving $R \sim 1000$ spectra across the full NIRSpec wavelength coverage. At the time of writing, the latest JADES data release is described in F. D'Eugenio et al. (2024), which is Data Release 3.

For all practical purposes, the PRISM/CLEAR observations maximize the chances of detection of the continuum and emission lines, and the medium-resolution gratings' observations further enhance the accuracy of the measured redshift and provide more kinematic information and help separate key multiple emission lines that otherwise appear to be blended in PRISM spectra. Since the main aim of this study is to measure UV continuum slopes directly from the spectra of high-redshift galaxies, we primarily use the $R \sim 100$ PRISM/CLEAR spectra across all tiers of JADES where the UV continuum flux is detected with a decently high signal-to-noise ratio (S/N > 5).

2.2 Publicly available data

In addition to JADES data, we also utilize the publicly available *JWST* Cycle 2 GO program 3215 (co-PIs: Eisenstein, Maiolino), which aimed to build upon JADES imaging and spectroscopy in the newly defined JADES Origin Field (D. J. Eisenstein et al. 2023b), which lies 8 arcmin away from the HUDF in GOODS-S and was repeatedly observed as part of JADES observations in Cycles 1 and 2. We note here, however, that the NIRSpec MSA (microshutter assembly) observations taken as part of PID 3215 cover the same region as in PID 1210, overlapping the HUDF.

The technical setup of the spectroscopic observations carried out as part of program 3215 is identical to the other JADES observations, with the same filter/disperser combinations being used. This enables a large degree of homogeneity between the JADES observations and those from program 3215.

2.3 Spectroscopic redshift measurement

Detailed information about all the steps involved in obtaining spectroscopic redshifts for our spectroscopic targets can be found in F. D'Eugenio et al. (2024). However, in this section, we briefly describe the main steps involved in obtaining reliable spectroscopic redshifts. The redshift measurement procedure followed two steps. The first step involved obtaining a best-fitting spectral model to the observed spectrum using BAGPIPES (A. C. Carnall et al. 2018) on the PRISM data. Armed with the BAGPIPES redshift, each spectrum was then visually inspected by at least two members of the JADES team, particularly focusing on the simultaneous detection of two or more strong emission lines at the same redshift.

Additional input was also taken from the higher resolution grating spectra to further refine both the line detection as well as redshift determination for all sources where emission lines were detected in the grating spectra. Based on the detection (or lack thereof) in both the PRISM and the grating data, a number of quality and reliability flags were then assigned to each source, which are described in F. D'Eugenio et al. (2024). In particular, flags 6, 7, and 8 were used to identify 'robust' redshift measurements thanks to the detection of multiple lines, which is what we largely use in this study. At the highest redshifts (e.g. $z > 9.5$) when most bright rest-frame optical emission lines redshift out of the NIRSpec coverage, a redshift was determined mainly using the Lyα-break feature in the continua. However, for galaxies at these high redshifts, additional insights on the validity of their spectroscopic redshift are obtained from multiband NIRCam imaging and SED fitting, which effectively rules out these sources being low-redshift interlopers (e.g. K. N. Hainline et al. 2024).

2.4 Final sample selection

We note that the selection function of JADES, as is the case with the vast majority of NIRSpec programs utilizing the MSA can be inhomogeneous across redshifts. This is mainly because of the way that shutters are allocated to higher priority targets and the need to 'protect' these high-priority targets from spectral overlap originating from other nearby sources. This exercise naturally results in the highest priority class sources (e.g. at the highest redshifts) being more 'complete' than sources with lower priority classes, which may be excluded from shutters to avoid contamination.

For JADES, as described in A. J. Bunker et al. (2023a), sources at $z \gtrsim 5$ (*i*-band dropout sources) were assigned systematically higher priorities than those at lower redshifts, resulting in a much higher fraction of such candidates ending up on MSA shutters. Sources at these redshifts are all mainly selected to be blue, star-forming galaxies (with the exception of a few 'oddball'-type objects with redder spectra), which results in further sample homogeneity favouring star-forming galaxies at high redshifts compared to lower redshifts, where a wider variety of galaxy types were placed in shutters.

The main driver, therefore, for the selection of Lyman-break galaxies at $z > 5$ is the flux-limited nature of the survey, which manifests itself as a UV magnitude selection as a function of redshift. At progressively higher redshifts, the probability of photometrically selected high-z dropout sources being placed in shutters increases, making JADES a highly targeted high-redshift galaxy survey (A. J. Bunker et al. 2023a). Therefore, to leverage relatively 'complete' samples for the analysis of rest-frame UV slopes of galaxies in this paper, we restrict our sample to galaxies with spectroscopic redshifts $z > 5$, which will result in a more homogeneous and complete sample of Lyman-break selected galaxies that generally trace star-forming systems. We note, however, that with MSA surveys it may not be possible to obtain spectra for fully complete flux-limited samples.

We also note that although a number of (candidate) AGN (active galactic nucleus) have been identified from the JADES data sets (e.g. R. Maiolino et al. 2023; J. Scholtz et al. 2023; J. Lyu et al. 2024), we do not explicitly exclude any such source as these numbers remain low compared to the number of star-forming galaxies, and particularly for low-luminosity AGN, the rest-frame UV light may still be dominated by young stars and/or nebular continuum emission.

2.5 UV slope measurement

To measure the UV slopes, β, from the PRISM/CLEAR $R \sim 100$ spectra of all galaxies with robust spectroscopic redshifts, we implemented a novel Monte Carlo method that takes into account pixel-by-pixel uncertainties. The first step involved de-redshifting the galaxy spectra. We then proceeded to fit a power law to the rest-frame spectrum of the galaxies in the wavelength range $1340 - 2700$ Å, which is a slight modification of the standard D. Calzetti et al. (1994) windows to take into account the low spectral resolution of PRISM spectra that leads to broadening of the emission lines. This wavelength range avoids both the Lyα break and the Balmer break features in the continuum as well. To avoid fitting regions containing strong emission lines, we masked the regions $1440 - 1590$, $1620 - 1680$, and $1860 - 1980$ Å. We note that the masked wavelength ranges are purposefully kept large to account for the broadening of the rest-UV lines due to the low resolution of the PRISM/CLEAR grating/disperser combination. We also note here that in the wavelength range used to measure β, the intergalactic medium (IGM) damping wing feature should not play an important role in affecting β unless the column densities are extremely high (e.g. K. E. Heintz et al. 2024).

Next, other outlying pixels (either due to other emission lines, residual cosmic rays or noise fluctuations) were masked out by using a sigma-clipping implemented at the 10σ level in the spectrum. Pixels with negative or zero flux were also masked, ensuring that the S/N of the neighbouring pixels is always large enough such that the negative values only indicate bad data points.

Our Monte Carlo approach to measure the UV slopes was then implemented as follows. We performed 500 iterations and measured β from each spectrum by fitting the power-law function, where the flux in each spectral pixel was independently perturbed by randomly sampling from the distribution of the pixel-level noise. This approach produces a large range of possible β-values compatible with the pixel noise distribution. The median β derived from the 500 iterations was set as the UV slope of the galaxy, with the standard deviation set as the 1σ error.

This β measurement approach was implemented for all galaxies with robust spectroscopic redshifts in our sample. Given the variable depth of the various tiers of observations used in this study and the relatively broad redshift range resulting in variable UV absolute magnitude limits, it was deemed essential to weed out the rather uncertain β measurements from our final sample before exploring their statistical distribution. Therefore, we opted to use an error threshold of 5 per cent to select our final sample corresponding to a $> 2\sigma$ accuracy, which meant that galaxies with β uncertainties larger than 5 per cent were rejected.

Several targets were observed across multiple JADES tiers, where often one of the observations belonged to a deeper tier. To remove duplicates, we retain only the spectrum that was observed as part of the deeper tier from all duplicate observations of the same target, which also resulted in a lower error on the β measurement. After removing duplicates, the final sample of $z > 5$ galaxies with robust redshifts and reliable β measurements across all tiers consisted of 395 galaxies. A breakdown of the final sample across different tiers of observations is given in Table 1.

The distribution of the UV absolute magnitudes measured at rest-frame 1500 Å ($M_{\rm UV}$) and redshift of all galaxies for which β could be reliably measured with $\Delta\beta < 5$ per cent is shown in the left panel of Fig. 1. In the right panel of Fig. 1, we show the histogram of β measured across our sample, finding a mean $\beta = -2.10$, median $= -2.15$ indicated by the dashed line in the figure, and standard deviation $= 0.40$.

Table 1. Number of $z > 5$ sources with reliable ($\Delta\beta < 0.1$) UV slope measurements belonging to different tiers/programs of JADES observations used in this study.

Tier	PID	*N*
GS Deep/*HST*	1210	39
GS Deep/*JWST*	1287	24
GS-3215	3215	22
GS Medium/*HST*	1180	41
GS Medium/*JWST*	1180	23
GS Medium/*JWST*	1286	114
GN Medium/*HST*	1181	55
GN Medium/*JWST*	1181	78
Total		395

2.6 Slit loss and path loss considerations

An important observational effect that can potentially impact the measurement of rest-frame UV slope directly from spectra are the slit losses, which occur when parts of the galaxy are outside of the MSA shutter, and path losses, which occur due to the point spread function (PSF) of NIRSpec being wavelength dependent. We note that from a detailed morphological analysis of all NIRCam detected sources within the JADES footprint with reliable photometric redshifts, C. Carreira et al. (2026) found that the median sizes of galaxies at $z > 5$ decrease steadily with increasing redshift, and that the large majority of sources are smaller than 3 kpc at $z > 5$, which corresponds to roughly 3 arcsec on the sky. To estimate the effect of slit losses, in Fig. 2 we show the semimajor axes measured for galaxies in our final sample from the latest photometric catalogues that were released as part of JADES DR5 (C. Carreira et al. 2026; B. E. Robertson et al. 2026), colour-coded by β measured from NIRSpec PRISM spectra.

We find that only 9 per cent of the objects in our final sample have semimajor axes larger than 0.2 arcsec, which is the nominal width of the MSA shutters, with the majority of them being at $z < 8$, and only one source in our sample has a semimajor axis larger than the height of the MSA shutter of 0.46 arcsec.[1] These larger objects also typically have $\beta > -2$, indicative of more evolved or dustier systems. For these extended objects, it is possible that the MSA shutter only samples a subregion of the galaxy, which may be biased towards certain properties such as young starburst regions, older stellar populations, dustier environments or enhanced nebular gas contribution, which may not necessarily be representative of the conditions in the entire galaxy.

With regards to the path loss corrections, it is known that the PSF changes by a factor of up to ~ 3 over the wavelength range $0.6 - 5.3$ μm, which is nominally corrected for by the data reduction pipeline. The NIRSpec JADES data reduction pipeline takes the intra-shutter position of each target into account, which is then used to compute the slit losses. The source is assumed to be a point source at the location of the input coordinates within the shutter, which works particularly well for high-redshift sources that are found to be generally small (e.g. K. Ormerod et al. 2024). Since the UV slope measurement is made from the bluest part of the spectral coverage that has more compact, well-behaved PSFs, the much larger effect of path losses at redder wavelengths should not present a large source of uncertainty when measuring β from the spectra.

[1] https://jwst-docs.stsci.edu/jwst-near-infrared-spectrograph/nirspec-instrumentation/nirspec-micro-shutter-assembly

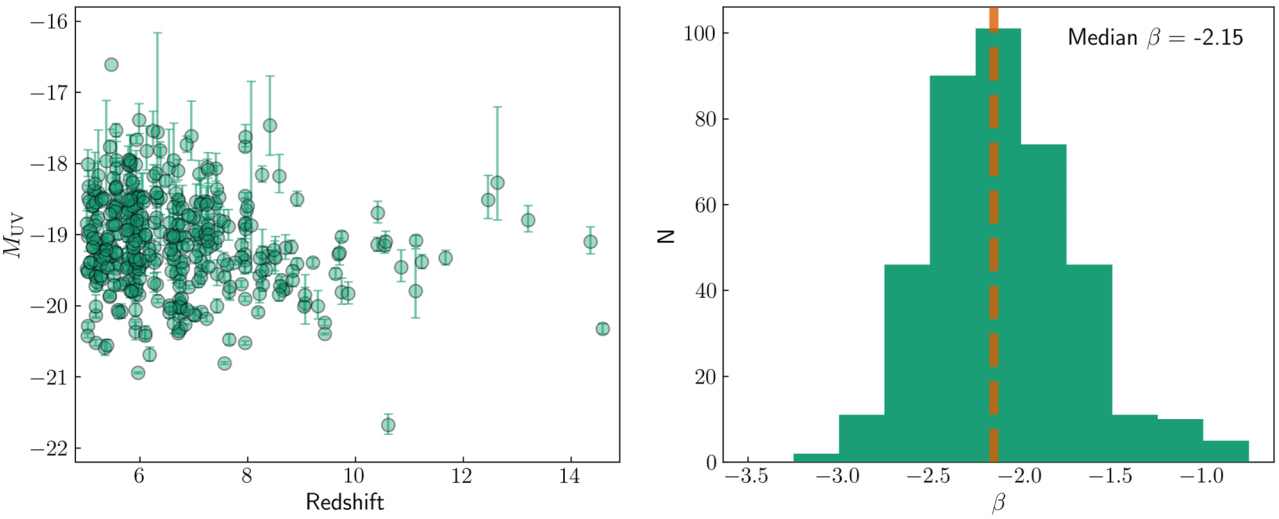

Figure 1. Left: overview of the spectroscopic sample considered in this study, which includes some of the highest redshift spectroscopically confirmed sources currently known. The continuum SNR > 2 requirement to measure the UV slopes ensures that the UV magnitudes are robustly measured for all galaxies in our sample. Right: histogram of the UV slope β of star-forming galaxies in this sample, with a median $\beta = -2.15$ indicated by the dashed line measured across our full sample.

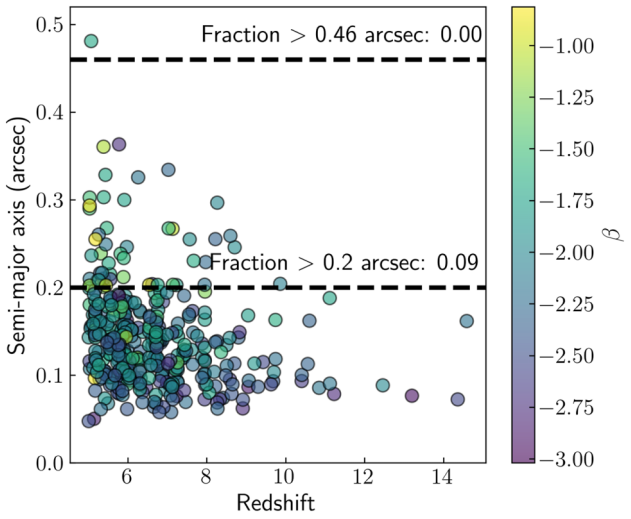

Figure 2. Distribution of the semimajor axis (C. Carreira et al. 2026; B. E. Robertson et al. 2026) measured for all galaxies in our final sample, colour-coded by the β measurement from NIRSpec spectra. The nominal width of the MSA shutter is 0.2 arcsec and height is 0.46 arcsec, which are marked using the dashed lines. We find that 91 per cent of the sources in our final sample are within the MSA shutter width, and only one source appears to be larger than the MSA shutter height, thereby minimizing the effects of significant slit/shutter losses and its impact on the UV slope measured from spectra.

However, to confirm the accuracy of β measurements from spectra in light of possible slit loss related biases, we verify that the flux measurements across wavelengths in the spectra are compatible with photometric fluxes measured from NIRCam. In other words, we would like to confirm whether the continuum flux densities measured in NIRSpec spectra, which are prone to slit/shutter losses, are consistent with fluxes measured using circular apertures from the NIRCam images to identify and remove any biases in the β measurements from spectra alone.

To do this, we computed synthetic NIRCam photometry for all spectra in our sample, and compared it with the CIRC2 NIRCam photometry (a circular aperture of 0.3 arcsec diameter, with an aperture correction applied appropriate for a point source) presented in M. J. Rieke et al. (2023). We found a remarkable agreement between the two flux measurements for the overwhelming majority of our sources, with outliers remaining few and far between. This finding confirms that (i) the slit loss corrections are largely being properly implemented in the data reduction and calibration pipeline and (ii) the β measurements directly from spectra are not being impacted by these slit losses that are unaccounted for. We note here that with the increasingly large PSF at longer wavelengths, any appreciable impact of slit losses will bias the measured UV slopes bluer, particularly at the highest redshifts.

2.7 Binning and stacked spectra

Although we can obtain a robust measurement of β as well as physical and chemical properties of galaxies across the entire sample from individual spectroscopic measurements, we are particularly interested in investigating the dependence of β on galaxy properties and the redshift evolution of UV slopes. To achieve this, we bin our sample in β and redshifts, and produce stacked spectra weighted by S/N in each bin, where the S/N is measured at rest-frame 1500 Å, to study how β is related to the various physical and chemical properties traced by spectroscopic indicators. S/N weighting leverages the ultradeep observations that were taken as part of JADES, which is able to achieve high S/N observations for relatively UV faint galaxies.

The binning in β and redshift space is performed keeping the following points in mind. Since the redshift of the source plays an important role in dictating which emission lines will be visible in the observed NIRSpec spectrum, we wanted to ensure that redshift bins uniformly sample the observed strong emission lines, while ensuring that each redshift bin contained a comparable total number of sources. As a result, the lowest redshift Bin 1 covers the range $5 < z < 6$, Bin 2 spans $6 < z < 7$, where the

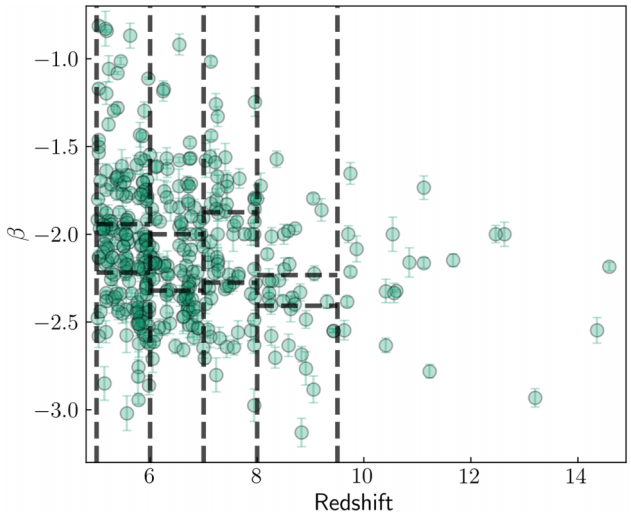

Figure 3. Binning of the sample in β and redshift space, chosen to produce stacked spectra and study the sample averaged evolution of β with redshift and other spectroscopic properties. The redshift bins were chosen to ensure coverage of key strong emission lines (as mentioned in the main text), whereas the β bins were simply chosen to split the sample into three equally numbered tertiles. We do not split our $z > 9.5$ sample into β bins to preserve number statistics in the stack.

Table 2. Sample splitting parameters in bins of redshift and β.

Bin	Redshift	Beta range	N
1A	$5-6$	$\beta > -1.94$	60
1B	$5-6$	$-1.94 > \beta > -2.22$	58
1C	$5-6$	$\beta < -2.22$	59
2A	$6-7$	$\beta > -2.00$	33
2B	$6-7$	$-2.00 > \beta > -2.32$	32
2C	$6-7$	$\beta < -2.32$	32
3A	$7-8$	$\beta > -1.87$	23
3B	$7-8$	$-1.87 > \beta > -2.28$	22
3C	$7-8$	$\beta < -2.28$	22
4A	$8-9.5$	$\beta > -2.23$	12
4B	$8-9.5$	$-2.23 > \beta > -2.41$	11
4C	$8-9.5$	$\beta < -2.41$	11
5	$z > 9.5$	All	21

cut-off at $z = 7$ is chosen such that all sources in this bin have Hα visible in their spectra, Bin 3 spans $7 < z < 8$, Bin 4 spans $8 < z < 9.5$, beyond which the [O III] and Hβ lines move out of NIRSpec wavelength coverage, and the highest redshift Bin 5 encompasses $z > 9.5$.

Within each redshift bin, we further split our sample into tertiles (three equally numbered bins) of β to effectively obtain three baseline β subsamples across redshifts. The resulting subsamples in β are as follows: Bin 1A: $\beta > -1.94$, Bin 1B: $-1.94 > \beta > -2.22$, and Bin 1C: $\beta < -2.22$, Bin 2A: $\beta > -2.00$, Bin 2B: $-2.00 < \beta < -2.32$, and Bin 2C: $\beta < -2.32$, Bin 3A: $\beta > -1.87$, Bin 3B: $-1.87 < \beta < -2.28$,and Bin 3C: $\beta < -2.28$, and Bin 4A: $\beta > -2.23$, Bin 4B: $-2.23 < \beta < -2.41$, and Bin 4C: $\beta < -2.41$. We note here that due to the presence of only 21 galaxies in our highest redshift Bin 5, we do not split this further in β and treat the $z > 9.5$ sample as a whole in this study. A visual representation of the bins in β-redshift space is shown in Fig. 3, with a breakdown of numbers in each subset of redshift and β given in Table 2.

We then produced stacked spectra in each bin in the following way. The spectra were first de-redshifted using accurate spectroscopic redshifts as mentioned earlier. The spectra in each bin were then resampled onto the same wavelength grid. Owing to our multitiered final sample containing spectra of variable depths and noise levels, we opt to use an S/N-weighted average stacking approach, which effectively upweights spectra with higher S/N and downweights spectra with lower S/N. We note that due to the multitiered construction of our sample, the S/N is not only dependent on the luminosity of the source, but also the depth of the tier of observations. Therefore, an S/N-weighted stacking scheme offers the best option to equally capture the contribution of galaxies occupying a range of UV fluxes/luminosities. The final weighted averaged spectra were then produced for each bin, with all the spectra shown in Fig. A1.

For each stacked spectrum, we then performed a new measurement of β following the same methodology as described earlier. We additionally measured fluxes and ratios of key emission lines, which included Hα, [O III] λ4959, 5007, Hβ, Hγ + [O III] λ4363, and [O II] $\lambda\lambda$3727, 3729, which appears to be blended. Using these lines, we calculated the dust attenuation from the Balmer decrements, the O32 ([O III]/[O II]) ratio and the R23 ([O II] + [O III]/Hβ) ratio, from which information about the ionization parameters and metallicities could then be derived. The relevant measurements for all stacks are given in Table 3.

3 RESULTS

Having measured β for all galaxies in our sample, grouped them into bins created in the β and redshift space, and created stacked spectra in each bin to study the dependence of β on key galaxy spectroscopic properties, in this section we present some of the main findings of this study.

3.1 The redshift evolution of the UV slope

We begin by investigating the redshift evolution of β across our spectroscopic sample. A plot of β as a function of redshift is shown in the left panel of Fig. 4, with both individual measurements and median values measured in the redshift bins 1–5. The median and standard deviation of β that we measure in the redshift bins are as follows: Bin 1 ($z = 5.82$): $\beta = -2.21 \pm 0.38$, Bin 2 ($z = 6.61$): $\beta = -2.26 \pm 0.32$, Bin 3 ($z = 7.43$): $\beta = -2.35 \pm 0.42$, Bin 4 ($z = 8.60$): $\beta = -2.43 \pm 0.42$, and Bin 5 ($z = 10.51$): $\beta = -2.33 \pm 0.32$. We find a very mild evolution of β with redshift throughout the whole redshift range, with the best-fitting relation showing a relatively shallow slope of -0.03. The median values of β decrease monotonically between redshifts 5.5 to $\sim$ 7.5, but show a slight upturn in the bin $z > 9.5$.

To further explore this trend at $z > 9.5$, we also derive the evolution of β without Bin 5, finding a much bluer slope of the best-fitting relation of -0.08, as also shown in the left panel of Fig. 4. This steeper trend would have predicted that most $z > 9.5$ sources have much bluer β-values, and although some sources appear to align with this trend, the median value measured at $z > 9.5$ is roughly in 1σ tension with the predicted trend at $z < 9.5$. Although this tension is not strong, the apparent flattening of the relation between β and redshift at $z > 9.5$ is clear.

To further explore the distribution of β-values across redshifts, in the middle panel of Fig. 4 we show violin plots for the distribution of β in the redshift bins considered in this study. It is clear that particularly in the $6 < z < 7$ bin, we may be missing

Table 3. Median properties measured from the stacked spectra of galaxies in bins of redshift and β. The Bin IDs are assigned as follows: bins of increasing redshift are from Bin 1 to Bin 5, with each redshift bin split into three sub-bins of β from reddest (A) to bluest (C).

Bin	N	z	β	EW (Hα) [Å]	EW (Hβ) [Å]	EW ([O III]$_{\lambda,5007}$) [Å]	O32	R23	$E(B-V)$ [Hα/Hβ]	$E(B-V)$ [Hβ/Hγ]	$12+\log$(O/H)
1A	60	5.461	-1.69	452.9 ± 32.3	81.4 ± 11.6	441.3 ± 62.4	5.0 ± 0.1	8.4 ± 0.1	0.26	–	$8.06 \pm 0.10^{*}$
1B	58	5.545	-2.07	562.2 ± 40.0	93.1 ± 13.2	562.9 ± 79.6	7.7 ± 0.1	8.9 ± 0.1	0.20	–	$7.87 \pm 0.10^{*}$
1C	59	5.766	-2.44	930.2 ± 66.0	154.2 ± 21.8	760.7 ± 107.6	10.8 ± 0.6	7.1 ± 0.3	0.08	–	$7.96 \pm 0.15^{*}$
2A	33	6.550	-1.79	494.3 ± 35.2	104.0 ± 14.9	568.2 ± 80.4	6.0 ± 0.1	8.2 ± 0.2	0.10	–	$8.02 \pm 0.09^{*}$
2B	32	6.555	-2.18	706.8 ± 50.3	138.6 ± 19.7	771.4 ± 109.1	9.5 ± 0.3	8.0 ± 0.2	0.21	–	$8.10 \pm 0.09^{*}$
2C	32	6.666	-2.47	681.9 ± 48.5	143.6 ± 20.6	807.4 ± 114.2	9.8 ± 0.1	8.1 ± 0.1	0.00	–	$7.91 \pm 0.09^{*}$
3A	23	7.278	-1.69	–	151.6 ± 21.9	720.0 ± 101.9	5.9 ± 0.1	7.1 ± 0.2	–	0.26	$7.87 \pm 0.09^{\dagger}$
3B	22	7.513	-2.12	–	119.9 ± 17.1	661.3 ± 93.6	13.5 ± 0.5	11.6 ± 0.2	–	0.00	$8.14 \pm 0.09^{\dagger}$
3C	23	7.430	-2.54	–	160.8 ± 22.9	904.9 ± 128.1	16.0 ± 1.2	18.1 ± 0.4	–	0.00	$7.53 \pm 0.10^{\dagger}$
4A	12	8.547	-1.99	–	166.0 ± 23.8	915.2 ± 129.5	8.1 ± 0.3	7.5 ± 0.3	–	0.12	$7.70 \pm 0.09^{\dagger}$
4B	11	8.415	-2.36	–	128.5 ± 18.4	660.3 ± 93.5	12.2 ± 0.6	14.1 ± 0.3	–	0.00	$7.41 \pm 0.09^{\dagger}$
4C	11	8.836	-2.63	–	146.9 ± 21.8	677.0 ± 96.0	8.6 ± 0.6	8.6 ± 0.6	–	0.00	$8.20 \pm 0.10^{\dagger}$
5	22	10.604	-2.20	–	–	–	–	–	–	–	–

Notes.*denotes gas-phase metallicities measured using the strong line method (e.g. M. Curti et al. 2020) and † denotes metallicities measured using the direct T_e method from the [O III] λ4363 auroral line detection.

the tail of the distribution at the bluest β-values. This implies that in a more complete survey, the median β measured at these redshifts may be even bluer. The $z > 9.5$ bin on the other hand, despite suffering from low number statistics, appears to be a well-sampled normal distribution, giving further credibility to the idea of reddened β at $z > 9.5$. Lastly, we note that there are not many galaxies with $\beta < -3.0$ across the full redshift range, contrary to what has been reported by studies relying on photometric measurements of β at these redshifts.

At $z > 9.5$ in Bin 5, we find that the vast majority of galaxies have $\beta < -2$, consistent with stellar ages being relatively young, with recent star formation and low dust content. We only see one galaxy with $\beta \sim -3$ at $z > 9.5$, which is possibly tracing extremely young, stellar-light-only dominated conditions with no dust attenuation. We will return to the properties of $z > 9.5$ galaxies as inferred from their β slopes and other spectroscopic indicators in the discussion.

Overall, we find a milder evolution of β with redshifts when compared to the results from F. Cullen et al. (2023b). However, we note here that the F. Cullen et al. (2023b) sample contained many more $z > 10$ sources, although with only photometric redshifts. In particular, at $z > 8$, we actually find a somewhat flipped trend compared to F. Cullen et al. (2023b). We note that at $z > 10$, we do not have any β measurements bluer than -3, whereas ~ 20 sources in the F. Cullen et al. (2023b) sample have $\beta < -3$. Galaxies with photometric $\beta < -3$ at $z > 10$ were also reported in the photometric sample of F. Cullen et al. (2023a) and M. W. Topping et al. (2024), which may play a role in enhancing the observed increase in blueness of β with redshift. We also note that the typical uncertainty on the measurement of β in our study is ± 0.1, whereas for most photometric studies it is ± 0.4.

3.2 Dependence of the UV slope on UV magnitude

Next, we investigate the dependence of β on the UV magnitude of our galaxies. In the right panel of Fig. 4, we show the distribution of β with $M_{\rm UV}$, with median values measured in quartiles of $M_{\rm UV}$ in our sample also shown. The median β that we measure in $M_{\rm UV}$ bins, from brighter to fainter, for all redshifts are as follows: $M_{\rm UV}$Bin 1 ($M_{\rm UV} = -20.24$): $\beta = -2.06 \pm 0.39$, $M_{\rm UV}$Bin 2 ($M_{\rm UV} = -19.39$) = $\beta = -2.15 \pm 0.36$, $M_{\rm UV}$Bin 3 ($M_{\rm UV} = -18.58$): $\beta = -2.16 \pm 0.44$, and $M_{\rm UV}$Bin 4 ($M_{\rm UV} = -17.76$): $\beta = -2.26 \pm 0.44$.

Overall, we find that β becomes bluer at fainter $M_{\rm UV}$ with a slope of -0.07 and a large scatter. This $M_{\rm UV}$ dependence is consistent with what has been reported from other photometric samples (e.g. F. Cullen et al. 2023a, b; M. W. Topping et al. 2024), in line with expectations that UV-fainter (or lower mass) galaxies must have fairly short, bursty, and recent star formation histories and/or lower dust content D. Narayanan et al. (e.g. 2024). Increased dust attenuation expected at brighter $M_{\rm UV}$ (or stellar masses) is likely playing a role in reddening the UV slope.

We further investigate the dependence of β on $M_{\rm UV}$ in our five independent redshift bins, as shown in Fig. 5. To do this, we split the sample in redshift Bins 1, 2, and 3 into $M_{\rm UV}$ tertiles (three equally populated bins), and Bins 4 and 5 into two sub-bins split by the median $M_{\rm UV}$. The subsets in $M_{\rm UV}$ in each redshift bins are as follows: redshift Bin 1: $M_{\rm UV} < -19.36$, $-19.36 < M_{\rm UV} < -18.76$ and $M_{\rm UV} > -18.76$, redshift Bin 2: $M_{\rm UV} < -19.40$, $-19.40 < M_{\rm UV} < -18.83$ and $M_{\rm UV} > -18.83$, redshift Bin 3: $M_{\rm UV} < -19.36$, $-19.36 < M_{\rm UV} < -18.86$ and $M_{\rm UV} > -18.86$, redshift Bin 4: $M_{\rm UV} < -19.51$ and $M_{\rm UV} > -19.51$, and redshift Bin 5: $M_{\rm UV} < -19.26$ and $M_{\rm UV} > -19.26$.

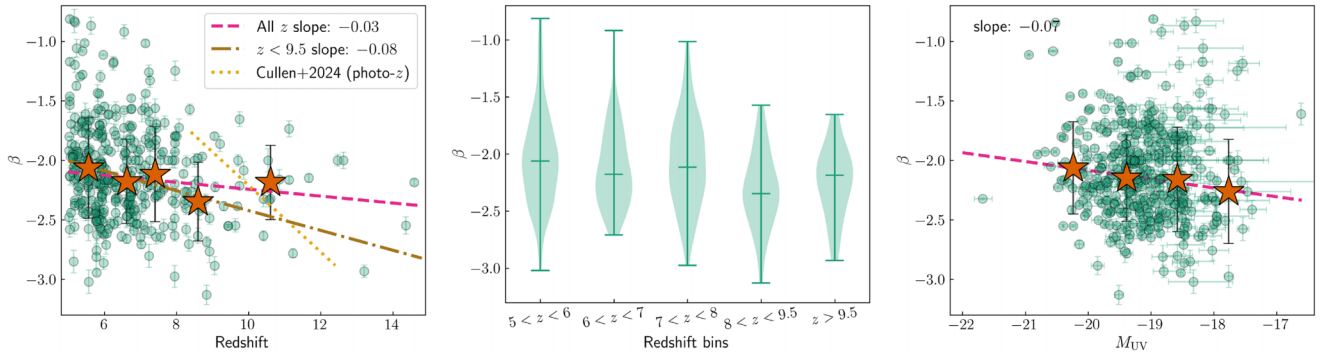

Figure 4. Left: β versus redshift, where the stars show the median and error bars show 1σ standard deviation in redshift bins. β becomes bluer between redshifts $z \sim 5.5 - 8$ but note that the β-values do not evolve much at $z \gtrsim 8$. The median and standard deviation of β measured in these redshift bins are given in the text. For reference, we also show the redshift evolution of β obtained by F. Cullen et al. (2023b) for a sample of $z > 8$ galaxies with photometric redshifts. Middle: violin plots showing the median and standard deviation for the distribution of β in the redshift bins considered in this study. We find that overall, the range of β-values is comparable across redshifts. At the highest redshifts, however, we do not see particularly red UV slopes ($\beta > -1.5$), but a slight reddening of the median β. Right: distribution of β versus $M_{\rm UV}$ for our sample, along with median β-values measured in $M_{\rm UV}$ quartiles measured across the full sample. The median and standard deviation of β measured in these $M_{\rm UV}$ bins are given in the text. We find a very weak dependence of β on $M_{\rm UV}$, with a shallow slope of the best-fitting relation of -0.05.

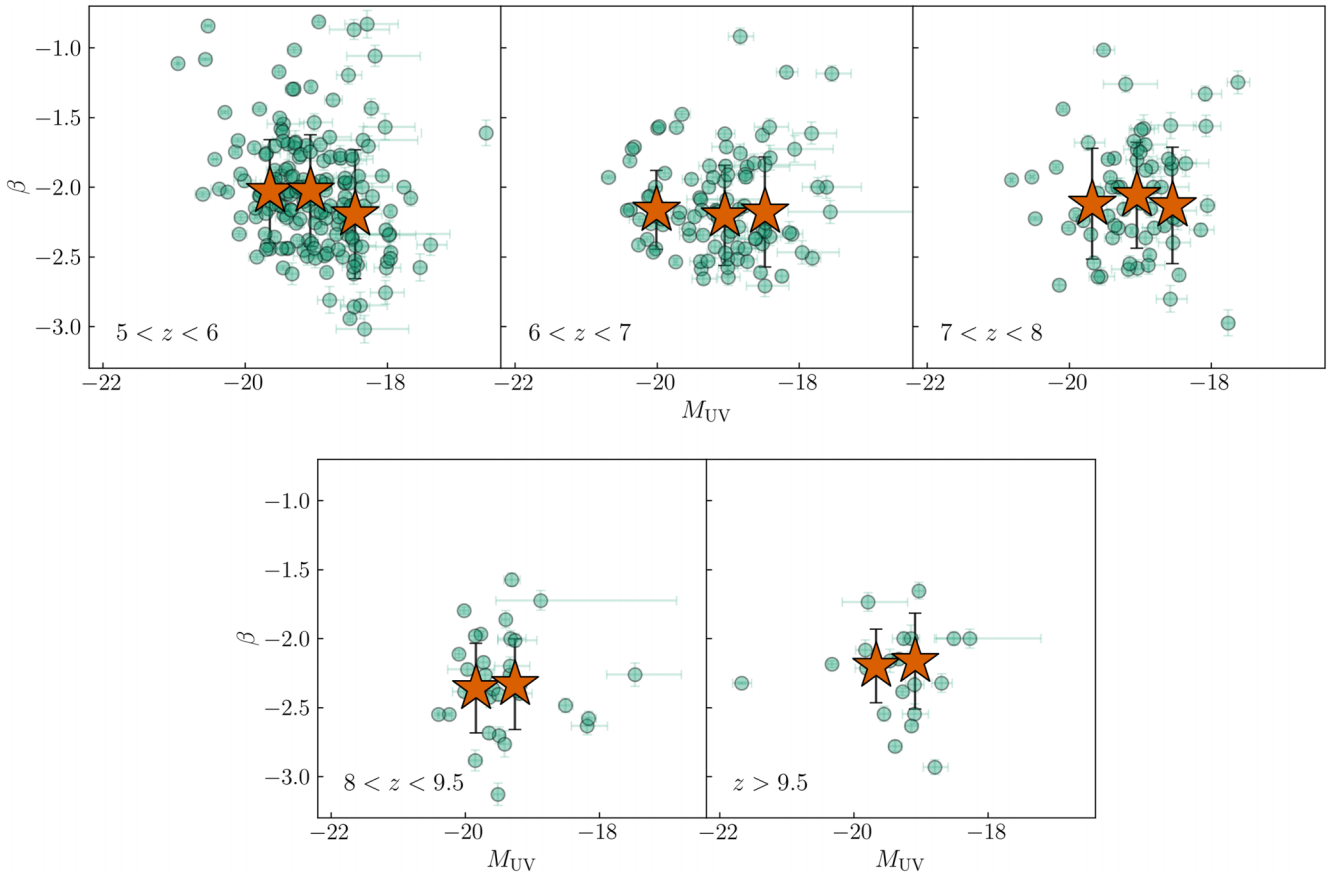

Figure 5. Dependence of β on the galaxy UV magnitude in different redshift bins. The error bars represent the standard deviation in the bins. At redshifts $5.5 < z < 6$ and $6 < z < 7$ we do see a clear correlation between β and UV magnitudes. However, there does not appear to be any dependence of β on UV magnitude at $z > 7$. This may be indicative of a lack of significant dust attenuation and its appreciable impact on the UV slopes of galaxies at $z > 7$.

In Bin 1 ($5 < z < 6$), we see an increase in blueness of β at fainter $M_{\rm UV}$, indicating that either (i) low-luminosity galaxies have high specific star formation rates that drive bluer β-values (D. Narayanan et al. 2024), and/or (ii) high-luminosity galaxies have a higher dust content, thereby reddening the β at the brighter end of the $M_{\rm UV}$ distribution. S. M. Wilkins et al. (2013) indeed showed that increasing dust attenuation can explain the relationship between β and $M_{\rm UV}$ out to $z \sim 7$, where the do see this relationship clearly in our sample.

However in Bins 2, 3, and 4 at $z > 6$, we do not see clear trends between β and $M_{\rm UV}$. We note here that the flux-limited nature of our spectroscopic sample may lead to incompleteness at fainter $M_{\rm UV}$ at the highest redshifts, which results in a limited number of galaxies fainter than $M_{\rm UV} > -18$ found at $z > 6$. Regardless, the lack of dependence of β on $M_{\rm UV}$ could be attributed to the fact that dust attenuation in $z > 6$ galaxies may not be as significant as it may be at $z < 6$, when there has been enough cosmic time since the formation of the first stars for significant amounts of dust to be produced and grown.

The galaxies at $z > 6$ span a large range of β-values, ranging from ~ -1 to ~ -3. The $M_{\rm UV}$ range at these redshifts is also relatively well sampled, although as noted earlier there is a missing population of galaxies with $M_{\rm UV}$ fainter than -18. We do not find any galaxy with $\beta > -1.5$ at $z > 8$, suggestive of either a selection effect where no appreciable emission lines were detected in the spectroscopy to confirm their redshifts, or that galaxies at these epochs are in general not significantly reddened by dust. We also note that our $z > 9.5$ bin contains two galaxies that are extremely UV-luminous with $M_{\rm UV}$ brighter than -20, GS-z14-0 at $z = 14.3$ (S. Carniani et al. 2024) and GN-z11 at $z = 10.6$ (A. J. Bunker et al. 2023b), which show relatively red β-values of $\beta \sim -2.3$.

In the next section, we investigate the dependence of β on the physical and chemical properties of galaxies inferred directly from spectroscopy, to understand what physical conditions drive the observed relations of UV slope with redshift and $M_{\rm UV}$.

3.3 UV slopes and galaxy physical properties

We now explore the properties inferred from the stacked spectra in our β and redshift bins, and investigate the connection between β and galaxy physical properties. We remind the readers that our sample was split into five redshift bins, Bins 1 to 5, and three β bins, Bins A, B, and C within each redshift bin (Table 3). The majority of the (rest-optical) emission-line-based properties that we present in this section are only possible for bins 1–4, as the highest redshift bin 5 does not cover rest-frame optical lines and the UV lines are not well-detected.

3.3.1 Dependence on dust

To measure the dust attenuation, we make use of the Balmer decrements using the Hα, Hβ, and Hγ lines whenever clearly visible in the stacked spectra. Owing to the variable spectral resolution of the NIRSpec PRISM, the Hγ and [O III]λ4363 features appear to be heavily blended in the spectra at $z < 7$. However, at these redshifts the Hα line is visible, and the dust attenuation at $z < 7$ is calculated using the Hα and Hβ lines. The Hα line moves out of NIRSpec coverage at $z > 7$, which is also when the Hγ + [O III]λ4363 feature becomes less blended due to an increase in resolution at the redder part of the observed spectrum. For these galaxies, we use the Hβ and Hγ ratios to infer dust attenuation.

To calculate $E(B-V)$ from the Balmer lines, we use the standard dust-free case-B recombination assumption with a temperature of $T_e = 10\,000$ K and density $n_e = 300\,{\rm cm}^{-3}$ (D. E. Osterbrock & G. J. Ferland 2006). These assumptions give an intrinsic Hα/Hβ ratio of 2.86, and Hβ/Hγ ratio of 2.13. We note here that given recent T_e measurements from NIRSpec spectroscopy of galaxies at high redshifts (e.g. I. H. Laseter et al. 2024), the assumption of $T_e = 10\,000$ K may not be hot enough for such calculations, although this can be mitigated by the fact that the intrinsic value of the Balmer decrement does not change dramatically with temperature – the Hα/Hβ ratio at $T_e = 15\,000$ K for example is 2.79, representing only a 2.4 per cent change. Furthermore, it has been shown recently that Case-B recombination assumptions may not be valid across all high-redshift galaxies (e.g. W. McClymont et al. 2024; C. Scarlata et al. 2024; H. Yanagisawa et al. 2024), which will impact the amount of dust attenuation inferred from intrinsic ratios by up to 0.2 dex.

In the top-left panel of Fig. 6, we show the $E(B-V)$ measured from Balmer lines for each β–z bin as a function of β. Overall, we find a clear decrease in the dust attenuation measured from stacked spectra with increasingly bluer β-values. These observed trends help confirm that an increased dust attenuation contributes towards reddening the observed β across all redshifts. Galaxies with moderate to blue β at $z > 7$ exhibit virtually no dust attenuation, consistent with expectations from models and simulations (e.g. D. Narayanan et al. 2024).

3.3.2 Dependence on gas-phase metallicity

We measure the metallicities from the stacked spectra in each bin using both the strong line method and the direct-T_e method, which relies on the robust detection of the [O III]λ4363 line. As noted in the previous subsection, the Hγ + [O III]λ4363 feature is heavily blended at $z \lesssim 7$ in PRISM spectroscopy, preventing us from inferring the electron temperature from the [O III]λ4363/[O III]λ5007 ratio. At higher redshifts, however, the measurement of T_e is easier. Therefore, at $z < 7$, we infer the metallicity 12 + log(O/H) using the strong line method, and for all other bins we employ the direct-T_e method.

Strong line metallicities were inferred from the R23 ratio using the calibrations derived by M. Curti et al. (2020). For the direct-T_e method, we assume a density $n_e = 300\,{\rm cm}^{-3}$ and derive the electron temperature T_e using the grids provided in PYNEB (V. Luridiana, C. Morisset & R. A. Shaw 2015).

It is common to assume that the electron temperature of the region from which the Hβ emission originates is the same as of [O III], but certain scaling relations need to be used to estimate the temperature of the [O II] emitting gas when the [O II] auroral line is not clearly detected in the spectrum (e.g. A. J. Cameron, H. Katz & M. P. Rey 2023b). To estimate T([O II]), we use the scaling relations presented in E. Pérez-Montero (2017), using the density dependent relation derived by G. F. Hägele et al. (2006) assuming $n_e = 1000\,{\rm cm}^{-3}$.

In the top-right panel of Fig. 6, we show the interdependence between β across redshifts and the gas-phasE OXYGEN ABundance (measured as 12 + log(O/H)) inferred from stacked spectra. As expected, we see an overall trend of decreasing metallicity at increasing redshifts, which has already been reported in the literature using *JWST* spectroscopy (e.g. M. Curti et al. 2023; K. Nakajima et al. 2023; R. L. Sanders et al. 2023; G. Roberts-Borsani et al. 2024). Interestingly, we do not see any clear dependence between oxygen abundance and β across any of our redshift bins, indicating that the gas-phase metallicity may not be a key driver of the observed β in high-redshift galaxies (see also E. Curtis-Lake et al. 2023, for example).

We note here that the β arising from especially young, metal-poor stellar populations would require low stellar metallicities, which may not necessarily be reflected in the gas-phase metal-

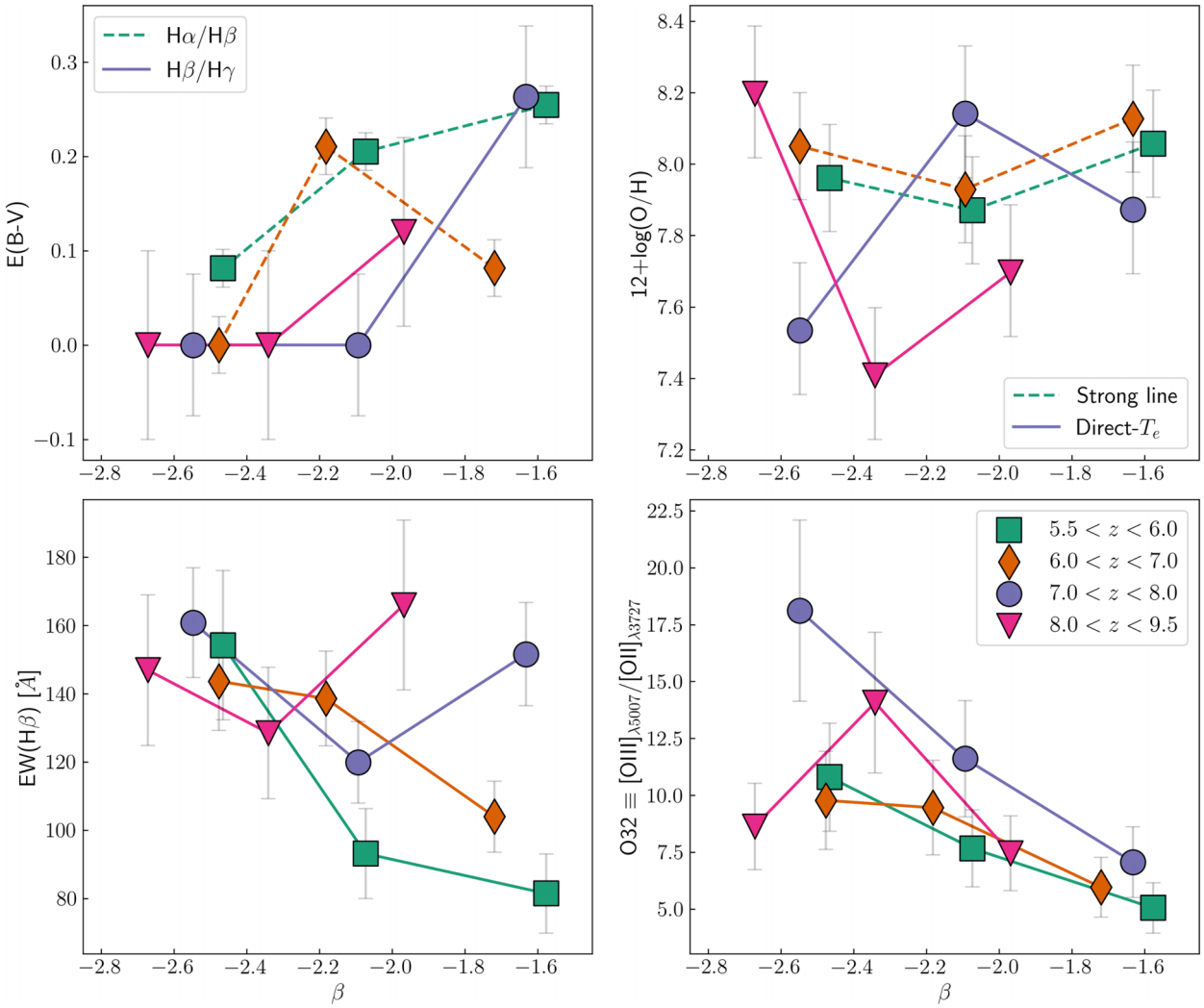

Figure 6. Clockwise from top left: dependence of galaxy properties such as dust attenuation or $E(B-V)$ (top-left), gas-phase metallicity given by 12 + log(O/H) (top-right), O32 ratio (bottom-right), and the Hβ EW (bottom-left) on the β measured from stacked spectra in bins of redshift and β. The redshift bins are represented by different symbols and are used consistently across all panels. We find that dust attenuation measured using Balmer decrements of both Hα/Hβ (dashed line) and Hβ/Hγ (solid line) decreases at bluer β-values, with little to no dust seen in the stacked spectra of our highest redshift bins. The metallicity, which we have measured using the strong-line method for the lowest redshift bins (dashed line) and direct-T_e method (solid line) for the higher redshift bins, does not show any appreciable trend with β. The O32 ratio generally appears to increase at bluer β-values tracing younger stellar populations, but interestingly shows a downturn at the bluest β-values at the highest redshifts, which could be explained by a turbulent ISM in galaxies with the bluest UV slopes (e.g. Y. Jin, L. J. Kewley & R. S. Sutherland 2022). The Hβ EW also does not show any clear trend with β.

licities. When the gas surrounding stars is enriched by the first generation of stars that formed out of chemically pristine gas, the gas gets polluted by heavier metals as soon as the first massive star winds and supernovae occur. Importantly, the gas-phase 'metallicity' that we measure and report here is simply the oxygen abundance in the gas measured via emission lines. This is in contrast to the stellar metallicity, which usually reflects the level of iron enrichment among other heavier elements (see F. Cullen et al. 2021, for example). Therefore, the gas-phase oxygen abundance may not be a good tracer of the metallicity of the underlying stars that are producing the ionizing radiation and largely setting the β-values. Therefore, gas-phase metallicities would not be expected to correlate very strongly with β, which is what we find from our data.

3.3.3 *Dependence on O32 ratio*

Low-metallicity conditions where young stars are forming generally result in higher ionization parameters that often lead to higher O32 ratios (e.g. A. E. Jaskot & M. S. Oey 2013; M. Paalvast et al. 2018). From measurements across our stacked spectra, we find a clear increase in the O32 ratio at bluer β-values, as can be seen in the bottom-right panel of Fig. 6. However, we note that for the redshift $8 - 9.5$ bin, there is a significant decrease in the O32 ratio for the bluest β bin, while the highest O32 ratio is seen in the intermediate beta bin. Although this observation could simply be a statistical effect, the dramatic decrease seen in the measured O32 ratio in this bin warrants qualitative discussion about its possible causes, which we briefly discuss below.

One possible pathway to lower the O32 in the presence of a young, highly ionizing and dust-free stellar population is by altering the geometry of the H II regions. Y. Jin et al. (2022) showed that increased turbulence can decrease the O32 ratio along certain lines of sight when making spectroscopic observations by apparently boosting the relative contribution of the lower ionization emission lines such as [O II], originating from the outer parts of the H II region (see also H. Katz et al. 2022). A turbulent ISM (interstellar medium) with a fractal-like geometry could increase the surface area covered by the 'edges' of the ionization front, as opposed to what would be expected assuming a simple spherical geometry, which can increase the fractional volume of the H II region that has a lower ionization state when observed at certain viewing angles. These differences are expected to be particularly pronounced in spatially resolved spectroscopy. Density and temperature fluctuations in the ISM have indeed been shown to change the inferred properties of the ISM from emission-line diagnostics (e.g. A. J. Cameron et al. 2023b) due to line-of-sight effects, and such effects are typically not captured by simple spherically symmetric models of emission from H II regions. Turbulence in the ISM may be expected in galaxies where a very recent or extreme starburst event has taken place, traced by the observed extremely blue UV slopes.

It may also be possible that the low O32 ratio in the bluest β bin at $8.0 < z < 9.5$ may be tracing non-turbulent, ionization-bounded H II regions, as opposed to a density-bounded nebula that is typically seen in high-redshift galaxies with strong underlying sources of ionization. In an ionization bounded scenario, the [O III] emission dominates closer to the ionizing source where the gas is in a higher ionization state, and the [O II] emission dominates further away from the source where gas is in a lower ionization state. However, in ionization bounded nebulae with no ionizing photon escape, the Balmer emission lines arising from recombination (Hα, Hβ) appear to be strong. As we will explore in the next subsection, we do find that EW(Hβ) in the bluest β bin at $8.0 < z < 9.5$ is higher than that seen in the intermediate β bin at this redshift, suggesting ionization bounded H II regions as a likely explanation of the decrease in O32.

3.3.4 Dependence on EW(Hβ)

The rest-frame equivalent width (EW) of the Hβ line (along with other Balmer recombination lines) has been shown to be a good tracer of stellar ages, as the decrease in ionizing photon flux with increasing stellar age leads to the depletion of the nebular component of the Balmer emission lines (e.g. C. Leitherer 2005; E. M. Levesque & C. Leitherer 2013). How the EW(Hβ) actually decreases with increasing age, however, depends on a number of factors such as the metallicity and the dust content and geometry of H II regions, stellar rotation, and whether massive stars are formed in binaries. Another important parameter that can reduce the observed Hβ flux is the escape of hydrogen ionizing LyC photons.

In the bottom-left panel of Fig. 6 we show the distribution of EW(Hβ) measured from our stacked spectra with β. At $z < 7$, we find a clear increase in EW(Hβ) with increasing blueness of β, indicating that galaxies with bluer UV slopes are likely powered by relatively younger stellar populations that are capable of producing a larger number of hydrogen ionizing photons. At $z > 7$, however, we find that the reddest and the bluest β bins show high values of EW(Hβ), but the intermediate β bins show much lower values.

The observed trends at $z > 8$ indicate that a more complex scenario may be at play in these relatively younger galaxies. The relative decrease in EW(Hβ) tracing the ionization of nebular gas even at intermediate β may be a result of ionization-bounded H II regions with little to no LyC photon escape as discussed in the previous subsection. Conversely, this could be a result of increasingly non-zero escape fraction of LyC photons from galaxies with intermediate β at $z > 8$, which effectively removes ionizing photons that would otherwise have ionized the hydrogen gas in the galaxy H II regions, depositing them instead in the galaxy circumgalactic medium (CGM) and/or IGM, driving the process of reionization (e.g. M. W. Topping et al. 2022).

3.4 Extremely blue UV slopes: $\beta \leq -2.9$

From our sample of 395 galaxies at $z > 5$, we identify five galaxies that show extremely blue UV slopes with $\beta \leq -2.9$, which are likely tracing extremely young stellar populations, conditions that may enable high LyC escape fractions (e.g. M. W. Topping et al. 2024) and/or extremely low stellar/gas-phase metallicities (e.g. M. Paalvast et al. 2018). These values of β are typically hard to reproduce using simple stellar population (SSP) synthesis models. In this section, we explore the individual spectra of these five sources in more detail, measuring the relevant spectroscopic properties to determine what set of physical and chemical conditions might be responsible for the observed extremely blue UV slopes.

We further estimate the LyC photon escape fractions ($f_{\rm esc}$) using the β-based prescription derived by J. Chisholm et al. (2022) as well as the multivariate $f_{\rm esc}$ estimation method derived using the SPHINX simulation by N. Choustikov et al. (2024a). The N. Choustikov et al. (2024a) method takes as input the Hβ luminosity, $M_{\rm UV}$, dust attenuation, O32 and R23 measurements, which are possible for our galaxies thanks to deep spectroscopy. We note that there are additional multivariate estimators of LyC $f_{\rm esc}$ available in the literature (e.g. S. Mascia et al. 2023; A. E. Jaskot et al. 2024), but given the available measurements for our sample we restrict ourselves to only the above-mentioned two approaches.

The galaxies in this section are presented in decreasing blueness of their UV slopes, and their 1D (in F_ν) and 2D spectra are shown in Fig. 7, with the best-fitting β slope also shown. For comparison, we further show the NIRCam photometry for these objects, which demonstrates how photometric bands crucial for measuring β photometrically may often suffer from emission line or continuum feature contamination, which can impact the inferred β.

3.4.1 JADES-GS-20192042

This galaxy was observed as part of the GS-JWST-DEEP tier, spectroscopically confirmed at $z = 8.836$ with $\beta = -3.13 \pm 0.08$ and a bright $M_{\rm UV} = -19.51^{+0.35}_{-0.52}$. Several strong rest-frame optical emission lines such as the [O III] doublet and Hβ are visible in its spectrum, with hints of strong UV lines such as C IV and C III]. There is a clear damped Lyα feature visible in the spectrum, which is also traced by the NIRCam photometry. Since the Hα line is our of NIRSpec coverage at this high redshift,

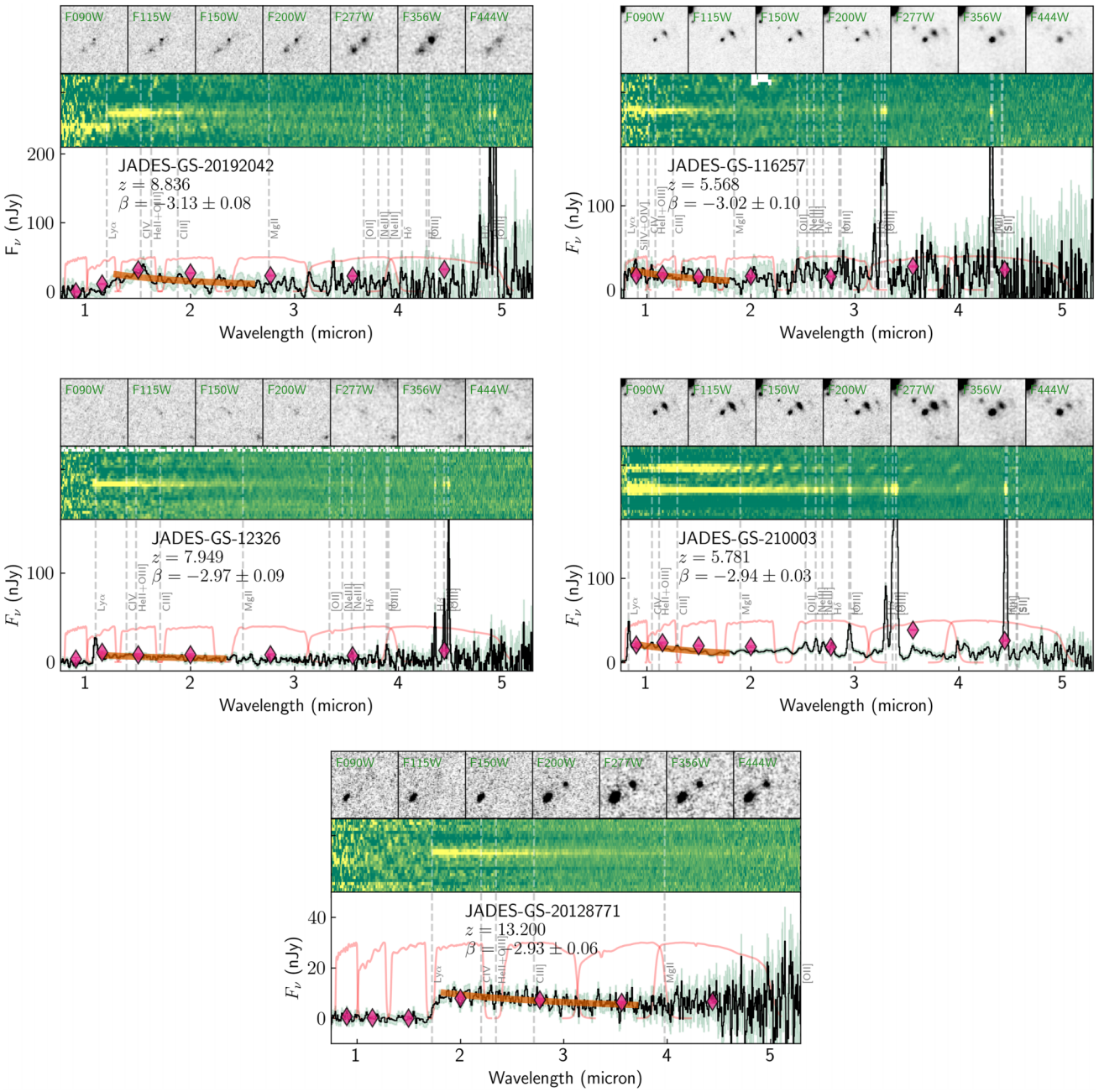

Figure 7. 1D and 2D spectra for galaxies in our sample that show the bluest β-values, with $\beta \leq -2.9$. Two of these galaxies show Lyα emission, which may be indicative of significant LyC escape as well (e.g. A. Verhamme et al. 2015). GS-210003 at $z = 5.779$ shows a very interesting spectrum, with clear detections of the Si IV + O IV] and He II + O III] complexes. The Si IV + O IV] complex in particular is not widely detected across galaxy spectra, and if the O IV] is high, it would signify the presence of extremely hard ionizing radiation fields.

we use the Hβ and Hγ emission lines to determine no dust attenuation.

This galaxy has a remarkably high O32 ratio of 22.5 ± 6.7 and a low R23 ratio of 5.7 ± 1.4. From the strong Hβ emission line, we measure a very high $\log(\xi_{\rm ion}/{\rm Hz\,erg^{-1}}) = 25.7 \pm 0.1$. Using the J. Chisholm et al. (2022) method that relies on β we estimate a very high $f_{\rm esc}({\rm LyC}) = 0.86 \pm 0.17$. Using the multivariate approach of N. Choustikov et al. (2024a), we find a relatively lower $f_{\rm esc}({\rm LyC}) = 0.24 \pm 0.05$. Both these measurements will designate this high-redshift galaxy has a strong LyC photon leaker. The Lyα damping wing, however, suggests the presence of dense clouds of neutral hydrogen along the line of sight.

3.4.2 JADES-GS-116257

This galaxy was observed as part of the GS-JWST-MEDIUM-1286 tier of JADES and has a $\beta = -3.02 \pm 0.10$ at $z = 5.567624$ giving $M_{\rm UV} = -18.32^{+0.51}_{-0.98}$. This galaxy has a very high EW([O III]) of 1890 Å, with a high O32 ratio of 11.3 ± 1.7 and low R23 of 6.3 ± 0.7. We also measure EW(Hα) $\approx$ 450 Å, which combined

with its relatively faint UV magnitude results in an extremely high $\log(\xi_{\rm ion}/{\rm Hz\,erg^{-1}}) = 26.0 \pm 0.1$, close to the theoretical limit expected from pure star formation. The [Ne III] lines are also seen in this spectrum, consistent with the presence of hard ionizing radiation fields irradiating the nebular gas. This galaxy shows no dust attenuation from the Balmer decrement measured using Hα, Hβ, and Hγ.

Owing to its relatively low redshift, the Lyα line falls in a noisier part of the spectral coverage of NIRSpec, and it therefore remains unclear whether there is strong Lyα present. From the higher resolution *G*140*M* spectrum, we see hints of a possible C IV P-Cygni profile emission line, and weak He II and O III] lines, although both of these are relatively uncertain. The high O32 ratio, high $\xi_{\rm ion}$ and blue β point towards the presence of a spectrum dominated by light produced by extremely young (less than a few Myr) stars forming in a dust-free environment.

The LyC $f_{\rm esc}$ estimates from the two methods used here differ once again, with the J. Chisholm et al. (2022) method predicting $f_{\rm esc}({\rm LyC}) = 0.63 \pm 0.13$ whereas the N. Choustikov et al. (2024a) method predicts a lower $f_{\rm esc}({\rm LyC}) = 0.36 \pm 0.07$. Given the extremely high EW of the nebular emission lines, and the extremely high $\xi_{\rm ion}$, a lower LyC $f_{\rm esc}$ may be preferable so that a large fraction of ionizing photons is available to excite this strong line emission as opposed to leaking out of the galaxy into the CGM/IGM.

3.4.3 *JADES-GS-12326*

This source was observed as part of the deeper GS-JWST-DEEP tier, confirmed at $z = 7.95477$ with $\beta = -2.97 \pm 0.12$ and a relatively faint $M_{\rm UV} = -17.76^{+0.10}_{-0.10}$. The PRISM spectrum shows an extremely strong and asymmetric Lyα emission line with EW(Lyα) 220 ± 40 Å, making it one of the highest redshift Lyman-alpha emitting galaxies (LAEs) currently known in the epoch of reionization (e.g. A. Saxena et al. 2024; J. Witstok et al. 2024), which is likely tracing a large ionized bubble (e.g. A. Saxena et al. 2023; J. Witstok et al. 2023). Based on the Hβ flux and assuming Case B recombination and no dust attenuation, we measure $f_{\rm esc}({\rm Ly}\alpha) = 0.82 \pm 0.11$.

This galaxy further shows strong [O III] and Hβ lines with no continuum detected in the rest-frame optical, giving EW([O III]) > 475 Å, with no [O II] emission seen in the spectrum, giving a limit of O32 > 10.2 and R23 < 5.9 suggestive of an extremely high ionization parameter and relatively low O/H abundance. From the Hβ emission line assuming no dust, we measure an extremely high $\log(\xi_{\rm ion}/{\rm Hz\,erg^{-1}}) > 25.9$.

The J. Chisholm et al. (2022) method predicts $f_{\rm esc}({\rm LyC}) = 0.55 \pm 0.11$ and the N. Choustikov et al. (2024a) method predicts $f_{\rm esc}({\rm LyC}) = 0.31 \pm 0.06$. The same arguments that were used for the previous galaxy could be applied here, where a lower $f_{\rm esc}$ may be preferable given the strong [O III] nebular line emission seen as well as the high $\xi_{\rm ion}$ inferred from the Hβ emission. The presence of strong Lyα emission may further be indicative of significant $f_{\rm esc}$(LyC), owing to the strong correlations reported between $f_{\rm esc}({\rm Ly}\alpha)/{\rm EW(Ly}\alpha)$ and $f_{\rm esc}$(LyC) both using observations of local analogues of high-redshift star-forming galaxies (e.g. S. R. Flury et al. 2022) and from high-resolution simulations employing radiative transfer (e.g. N. Choustikov et al. 2024b). Unfortunately, the Lyα line in the higher resolution *G*140*M* falls in the detector chip gap, which makes it impossible to infer the Lyα velocity offset compared to the systemic redshift, which is also a good indicator of the LyC $f_{\rm esc}$.

3.4.4 *JADES-GS-210003*

Observed as part of GS-3215, this galaxy at $z = 5.77885$ has $\beta = -2.94 \pm 0.03$, $M_{\rm UV} = -18.52^{+0.06}_{-0.06}$ and a strong Lyα line with EW$_0$(Lyα) $= 67 \pm 8$ Å, comparable to the sample of LAEs presented by A. Saxena et al. (2024). The much deeper exposure times in this tier result in high S/N detections of a host of rest-frame UV and optical emission-line features, including very strong [O III] λ5007 line with EW([O III]) $= 2930 \pm 930$ Å, O32 $= 22.5 \pm 2.5$ and R23 $= 5.6 \pm 0.5$. The strong Hα line has EW(Hα) $= 1720 \pm 610$ Å, giving an extremely high ionizing photon production efficiency, $\log(\xi_{\rm ion}/{\rm Hz\,erg^{-1}}) = 26.0 \pm 0.1$. There is no dust attenuation measured from the Balmer decrements. Using Balmer line emission, we calculate $f_{\rm esc}({\rm Ly}\alpha) = 0.17 \pm 0.02$, which is not as high as the previous source but still significant.

We note the presence of a possible contaminant in the 2D spectrum of this galaxy, which may have adversely affected the collapsed 1D spectrum from which the β was measured. In the observed spectrum, a slight deviation from a pure power law can be seen at wavelengths just longer than 2 μm, which could be due to contamination from the secondary source.

The spectrum also shows rest-frame UV features tracing high ionization conditions such as He II + O III] and C III], as well as a strong Si IV + O IV] emission, which is seldom seen in galaxy spectra with such high S/N. If there is indeed a strong contribution from He II and O IV] in the line complexes, this would signify the presence of extremely hard ionizing radiation sources, such as massive, hot stars, high-mass X-ray binaries, or even photoionization due to shocks (e.g. A. Saxena et al. 2020; M. Lecroq et al. 2024). The blue UV slope can help rule out photoionization from an AGN. Unfortunately, the He II and O III] lines fall in the detector chip gap in the *G*140*M* spectra that were also obtained, and therefore the complex cannot be resolved with higher spectral resolution.

The LyC $f_{\rm esc}$ derived from the J. Chisholm et al. (2022) method gives $f_{\rm esc}({\rm LyC}) = 0.50 \pm 0.10$, which is higher than that measured using the N. Choustikov et al. (2024a) method that gives $f_{\rm esc}({\rm LyC}) = 0.13 \pm 0.03$. Given the presence of high EW Lyα emission and a modest $f_{\rm esc}({\rm Ly}\alpha)$, this galaxy does appear to be a robust candidate LyC leaker.

3.4.5 *JADES-GS-20128771*

This galaxy, also named JADES-GS-z13-0 was originally confirmed spectroscopically at $z = 13.2$, via the characterization of its Lyman break, from the first ever pointing of JADES (E. Curtis-Lake et al. 2023), and then subsequently re-observed with deeper spectroscopy through the program GS-3215. From the deeper observations, galaxy has $\beta = -2.93 \pm 0.06$ and and a relatively bright UV magnitude for its redshift with $M_{\rm UV} = -18.79^{+0.16}_{-0.19}$, consistent with what was reported by E. Curtis-Lake et al. (2023). No other rest-UV emission lines are robustly detected in the spectrum, however, there is tentative evidence of C IV emission. Owing to its extremely high redshifts, the strong Balmer and oxygen lines are redshifted out of NIRSpec coverage. From the PRISM spectrum, we see strong evidence of damped Lyα absorption along the line of sight, suggesting that this galaxy is likely surrounded by neutral hydrogen, which is to be expected at these high redshifts.

Since no other lines are detected in the spectrum, the multivariate method of N. Choustikov et al. (2024a) cannot be used to determine its $f_{\rm esc}$(LyC). Using the β-based method of J. Chisholm

Table 4. Observed spectroscopic and derived properties of five galaxies in our sample that exhibit extremely blue UV slopes ($\beta \leq -2.9$) measured from their NIRSpec spectra. We note here that none of these galaxies show any signs of dust attenuation from their Balmer decrement measurements. C22 $f_{\rm esc}$(LyC) measurements are from the J. Chisholm et al. (2022) method, and the C24 measurements are derived using the N. Choustikov et al. (2024a) multivariate estimation method.

ID	z	β	$M_{\rm UV}$	$F(\rm H\beta)$ (erg s^{-1} cm^{-2})	O32	R23	$\log(\xi_{\rm ion})$ (Hz erg^{-1})	$f_{\rm esc}$(LyC) (C22)	$f_{\rm esc}$(LyC) (C24)
GS-20192042	8.83605	-3.13 ± 0.08	$-19.51^{+0.35}_{-0.52}$	$3.5 \pm 0.7 \times 10^{-19}$	22.5 ± 6.7	5.7 ± 1.4	25.7 ± 0.1	0.86 ± 0.17	0.24 ± 0.05
GS-116257	5.56762	-3.02 ± 0.10	$-18.32^{+0.51}_{-0.98}$	$6.1 \pm 0.8 \times 10^{-19}$	11.3 ± 1.7	6.3 ± 0.7	26.0 ± 0.1	0.63 ± 0.13	0.36 ± 0.04
GS-12326	7.94938	-2.97 ± 0.12	$-17.76^{+0.10}_{-0.10}$	$> 1.2 \times 10^{-19}$	> 15	< 5.5	> 25.9	0.55 ± 0.11	0.31 ± 0.06
GS-210003	5.78064	-2.94 ± 0.03	$-18.52^{+0.06}_{-0.06}$	$7.5 \pm 0.3 \times 10^{-19}$	22.5 ± 2.5	5.6 ± 0.5	26.0 ± 0.1	0.50 ± 0.10	0.13 ± 0.03
GS-20128771	13.20000	-2.93 ± 0.05	$-18.79^{+0.16}_{-0.19}$	–	–	–	–	0.49 ± 0.10	–

et al. (2022), we estimate $f_{\rm esc}(\rm LyC) = 0.49 \pm 0.10$. Given the lack of other spectroscopic indicators associated with LyC leakage, it is unclear whether this galaxy is leaking significant amounts of LyC photons or is simply powered by extremely young hot stars.

3.4.6 Concluding remarks

Overall, we find that galaxies with extremely blue $\beta \sim -2.9$ also on average show high O32 ratios, high $\xi_{\rm ion}$, and presence of other high-ionization emission lines in their spectra, in line with expectations from young, massive stars being the dominant producers of ionizing photons in the galaxies. Two out of the five galaxies show strong Lyα emission as well. The inferred LyC $f_{\rm esc}$ from the majority of these galaxies are high, in line with expectations that galaxies with blue UV slopes are good candidates for significant LyC leakage.

However, we note that the vast majority of these galaxies with extremely blue UV slopes also show strong nebular line emission, which is not to be expected if a large fraction of ionizing photons are escaping out of the ISM. This contradiction is somewhat represented in the discrepancy between the $f_{\rm esc}$(LyC) measured purely based on the UV slope, and by using multiple spectroscopic indicators that also take into account the state of the ISM. Therefore, if significant LyC leakage is not the main reason why the UV slopes of these galaxies appear so blue, the presence of low-metallicity stellar populations with extremely young ages offers a likely alternative explanation that is also consistent with strong nebular line emission, as we discuss in Section 4. In Table 4, we summarize the observed spectroscopic properties of these galaxies, and give the measured $\xi_{\rm ion}$ and LyC $f_{\rm esc}$ values as well.

4 UV SLOPES AT REDSHIFTS $z \gtrsim 9.5$

Having explored the connection between the UV slope and physical and chemical properties of galaxies at $z < 9.5$ primarily traced by various spectroscopic indicators, in this section we turn our attention to the UV slopes of galaxies at $z > 9.5$, where emission-line detections still remain few and far between.

4.1 Insights from simple stellar population models

Based on the statistical distribution of the measured UV slopes, it appears that the trend of increasingly bluer UV slopes as a function of redshift at $z < 9.5$ appears to become less significant at $z > 9.5$. Although there are selection effects at the highest redshifts that prevent the detection of UV-faint galaxies owing to the flux-limited nature of the spectroscopic surveys used here, the weak dependence of β on the UV magnitude even in more 'magnitude-complete' samples at lower redshifts in our sample suggests that incompleteness may not be the main cause of this reddening of UV slopes observed at the highest redshifts. The striking confirmation of a galaxy at $z = 14.32$ presented in S. Carniani et al. (2024) showing a remarkably red UV slope of $\beta \approx -2.3$ presents a compelling example. Therefore, in this section, we employ theoretical models to better understand the relatively red UV slopes seen across galaxies at $z > 9.5$.

The first step in employing models to understand the observations is to produce a library of synthetic galaxy spectra that can then be directly compared to the observations. To do this, we use the PYTHONFSPS code[2] (B. Johnson et al. 2024), which is a set of PYTHON bindings to the FSPS code[3] that allows the flexible modelling of stellar populations (C. Conroy, J. E. Gunn & M. White 2009; C. Conroy & J. E. Gunn 2010). Very briefly, FSPS allows the computation of SSPs for a wide variety of IMFs (initial mass functions), metallicities, ages and ionization parameters, including the addition of nebular continuum (N. Byler et al. 2017) and line emission. We use the standard installation of FSPS which uses the MIST isochrones (J. Choi et al. 2016; A. Dotter 2016) and MILES spectral library (P. Sánchez-Blázquez et al. 2006; J. Falcón-Barroso et al. 2011). We further include the WM-Basic hot star library from J. J. Eldridge et al. (2017) for stellar temperatures above 25 000 K.

For simplicity, we assume an SSP model with a single burst, with the burst age extending to 40 Myr, following a G. Chabrier (2003) IMF with an upper mass cut-off of 150 $\rm M_\odot$. In all models, we include Wolf–Rayet star spectra as well. The SSPs are created over a metallicity range $\log(Z_\star/\rm Z_\odot) = [-2.0, -0.5]$, and ionization parameters $\log(U) = [-3.0, -1.0]$. We also include trace amounts of dust with $E(B-V)$ values of 0.05 and 0.10, reflecting the level of dust attenuation seen in the $8 < z < 9.5$ bin from Balmer decrement measurements in Section 3.

In Fig. 8, we show example spectra with both stellar and nebular emission, and stellar only emission, for one of the models with $\log(Z/\rm Z_\odot) = -1.5$, $\log(U) = -2.0$, and age (time since burst) = 5 Myr. The vertical dashed lines indicate the wavelength range over which β is typically measured. No dust attenuation has been added to these models. Clearly, the inclusion of nebular continuum emission can redden the measured UV slope from $\beta = -3.0$

[2] https://dfm.io/python-fsps
[3] https://github.com/cconroy20/fsps

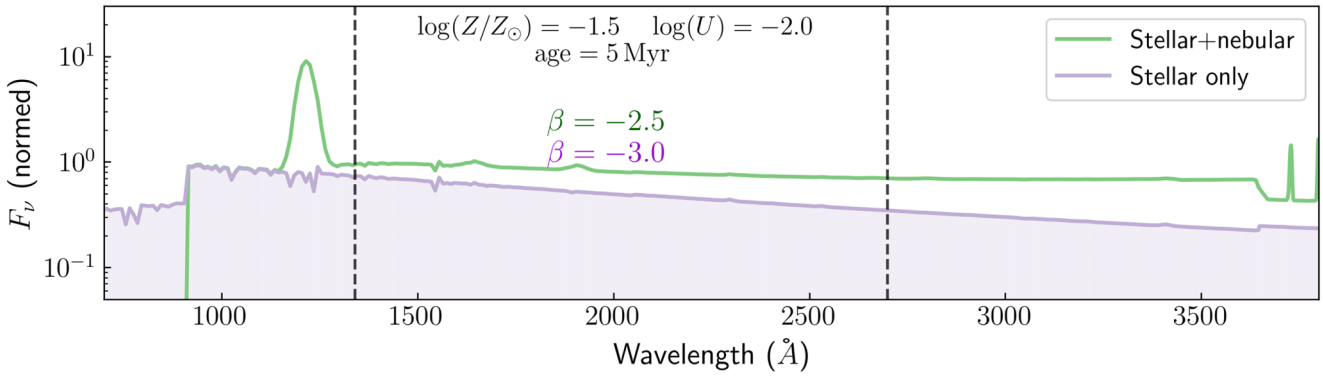

Figure 8. Synthetic spectra generated using PYTHONFSPS with both stellar and nebular emission (green) and stellar only emission (violet, shaded) for a SSP with $\log(Z/Z_\odot) = -1.5$, $\log(U) = -2.0$, and age (time since burst) = 5 Myr. The vertical dashed lines demarcate the wavelength range over which β is measured. It is clear that the inclusion of the nebular continuum reddens the measured UV slope to $\beta = -2.5$ compared to a stellar only value of $\beta = -3.0$. The impact of reddening the β due to nebular emission further depends on the physical and chemical conditions.

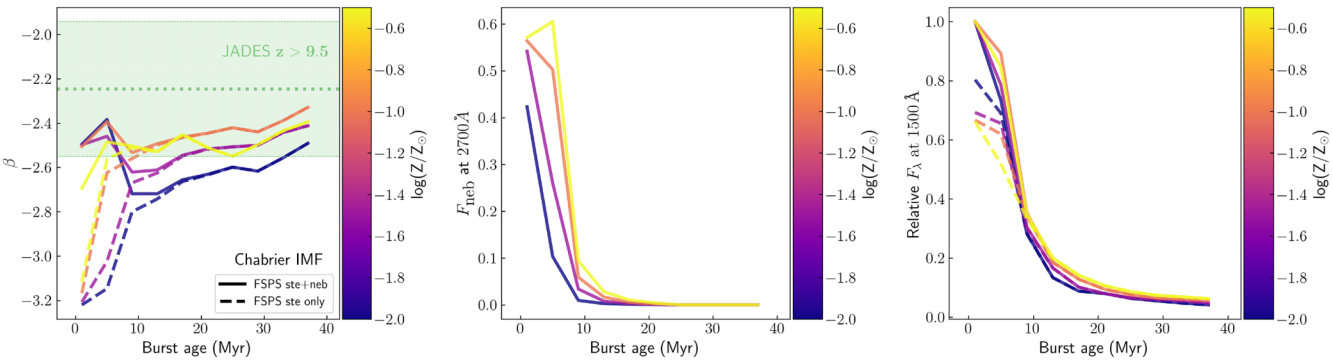

Figure 9. Left: β measured from synthetic spectra generated using FSPS with a Chabrier IMF as a function of age for a single burst of star formation with $\log(U) = -2.0$. Solid lines show measurements from spectra containing both stellar and nebular emission, and dashed line containing only stellar emission. The colour bar represents metallicities in units of $\log(Z_\star/Z_\odot)$. The dotted line is the median observed β for $z > 9.5$ galaxies in our sample, and the shaded region represents the 1σ dispersion. Middle: fraction of nebular continuum measured at 2700 Å, which leads to an overall reddening of the measured UV slope, as a function of burst age, colour-coded by metallicity. We find that at low burst ages, nebular emission can contribute up to 60 per cent of the flux in the redder part of the wavelength range where β is measured, thereby reddening the measured β-values. Right: the relative F_λ measured at 1500 Å from the model predictions, normalized at the maximum flux recorded in the stellar + nebular models at zero age. The nebular continuum for this particular IMF can provide a boost of up to 50 per cent to the UV luminosity at young ages. Overall, we find that redder β-values can also be achieved at burst ages > 30 Myr, but this is unlikely to be the case at $z > 9.5$ when galaxies are in the process of rapidly assembling their stellar masses through intense star formation.

for stellar only emission to $\beta = -2.5$ (see also D. Schaerer & R. Pelló 2005; S. M. Wilkins et al. 2013).

Having generated synthetic galaxy spectra for a variety of ages, metallicities and ionization parameters, we then measured the UV slope from these synthetic spectra in exactly the same way in which it was measured from observed spectra. As a result of this exercise, we have β measurements for synthetic spectra containing only stellar emission as well as stellar plus nebular emission, over a range of galaxy physical properties, which can now be compared with our observations at $z > 9.5$.

4.2 The role of nebular continuum

We begin by investigating the impact of the nebular continuum on the observed UV slope of galaxies. A substantial fraction of nebular continuum can redden the UV slope of galaxies, even in the presence of young, hot stars whose blackbody emission peaks at shorter wavelengths, as was also recently demonstrated by H. Katz et al. (2024) for a sample of galaxies where the rest-frame UV spectrum appears to be dominated by the nebular continuum. In the upper panel of Fig. 9, we show the β measured from synthetic spectra created following a Chabrier IMF as a function of time since burst for stellar only spectra (dashed lines) and spectra containing both stellar and nebular emission (solid lines) for $\log(U) = -2.0$ shown in the upper panel. The green dotted line marks the median β measured from our $z > 9.5$ galaxy sample, with the shaded region marking the 1σ deviation of the measurements.

It is clear that spectra that do not include any nebular contribution result in extremely blue UV slopes, particularly at early burst ages (see also F. Cullen et al. 2023b), which are incompatible with the median and 1σ dispersion of the measured β at $z > 9.5$ as shown in the left panel of Fig. 9. In the middle panel of Fig. 9, we show the evolution of the fractional contribution of nebular emission at 2700 Å, which generally represents the redder end of the wavelength range over which β is measured, as a function of time since burst. We find that nebular continuum contributes up to 60 per cent of the flux at 2700 Å (for this particular IMF

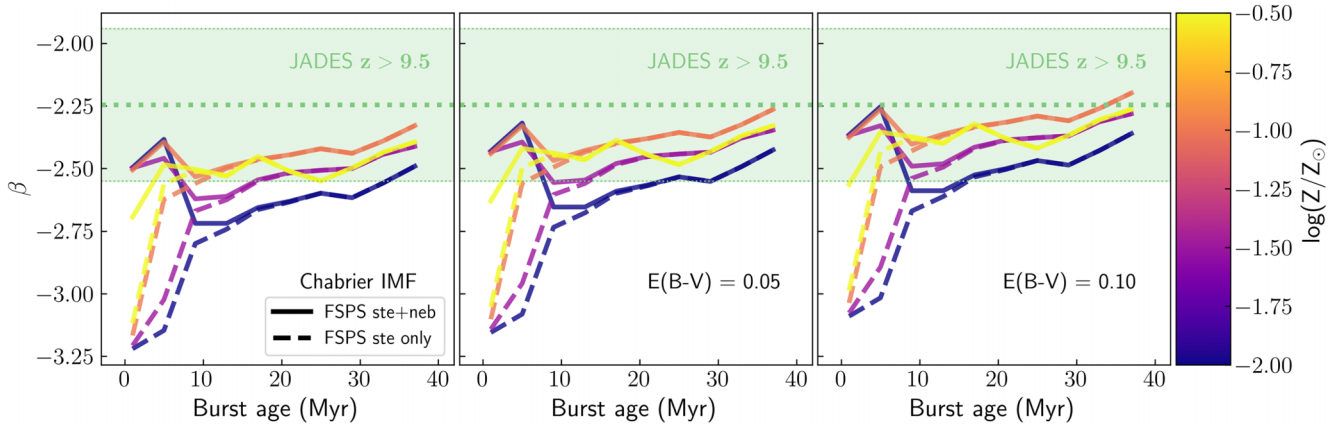

Figure 10. Same as Fig. 9, but here the different panels show the effects of dust attenuation (following the SMC attenuation law) on the UV slopes. The left panel shows the predictions from Chabrier IMF with no dust attenuation, the middle panel shows UV slope predictions with $E(B-V) = 0.05$ and the right panel for $E(B-V) = 0.10$. As expected, dust attenuation can redden the observed UV slopes, bringing the model predictions more in line with the measured UV slopes for our $z > 9.5$ sample.

and ionization parameter) at $\lesssim 10$ Myr, thereby reddening the measured β.

The β from stellar only and stellar + nebular models converges at burst ages greater than ~ 10 Myr, when the nebular emission peters out. The reduction of the nebular continuum also results in a dramatic decrease in the UV luminosity at 1500 Å for the same stellar mass formed, as shown in the right panel of Fig. 9. Therefore, to explain both the bright UV magnitudes and the red β-values seen in $z > 9.5$ galaxies in this work and across the literature, either younger stellar ages or the addition of stellar mass at higher ages would be needed. The metallicity of the nebular gas plays an important role in further reddening the β, with lower metallicities of $\log(Z_\star/Z_\odot) < -1.0$ producing redder UV slopes at < 10 Myr since the burst. The trend is reversed at higher burst ages when the nebular emission is less prominent, and higher stellar metallicities produce redder β-values owing to cooler stellar temperatures.

Insights into relatively bursty star-formation histories of early galaxies both from theory (e.g. C.-A. Faucher-Giguère 2018; S. Tacchella, J. C. Forbes & N. Caplar 2020; S. R. Furlanetto & J. Mirocha 2022; J. Mirocha & S. R. Furlanetto 2023; G. Sun et al. 2023) as well as observations of galaxies at the highest redshifts (e.g. R. Endsley et al. 2023; R. A. Meyer et al. 2024; M. W. Topping et al. 2024) have highlighted the important role that young stellar populations play in shaping the continuum and emission-line spectra of galaxies. Therefore, although higher stellar ages may be able to explain the relatively red β-values, as has indeed been seen in a handful of high-redshift galaxies characterized as 'mini'-quenched galaxies (e.g. T. J. Looser et al. 2024, 2025; W. McClymont et al. 2025; J. A. A. Trussler et al. 2025; C. Witten et al. 2025), based on the expected star formation histories of galaxies particularly at $z > 9.5$, increased fractional of nebular continuum driven by hot, massive forming stars may provide a more consistent explanation.

We find that none of the models can adequately explain the observed values redder than $\beta \gtrsim -2.3$, which is also what is measured for JADES-GS-z14-0 at $z = 14.3$ (S. Carniani et al. 2024). From a stellar populations perspective, it may be possible to further redden the observed UV slope by including a considerably older stellar population in the synthetic spectra, however, at $z > 9.5$ the Universe is less than 500 Myr old, and the existence of a dominant older stellar population already at these epochs may be in tension with expectations of first light in the Universe (typically expected to be $z \sim 20 - 30$). Furthermore, no clear evidence of Balmer breaks in the spectra of galaxies at $z > 9.5$ has yet been reported in the literature, casting doubt on the existence of a dominant older, more evolved stellar populations in these galaxies.

The inclusion of dust attenuation of the rest-UV flux is another channel by which the observed β-values could be reddened. S. Carniani et al. (2024) showed that trace amounts of dust may be needed to produce $\beta = -2.3$ in JADES-GS-z14. Furthermore, A. Ferrara (2024) recently proposed a scenario whereby galaxies can form a lot of stars very early in their lifetimes while being dust obscured leading to reddening of β, although this period lasts for a very short time before dust is eventually blown out by intense stellar feedback, making the UV slopes blue again. Therefore, in the following section we evaluate the role of dust attenuation in potentially reddening the UV slopes of $z > 9.5$ galaxies.

4.3 The role of dust

As shown in Fig. 10, dust attenuation with $E(B-V) \sim 0.1$ following the SMC (Small Magellanic Cloud) extinction law can redden the UV slopes emerging from young stars, bringing them in line with the observed distribution seen in our sample. Modest dust attenuation with $E(B-V) \sim 0.1$ was also seen from our measurements of the Balmer decrements in our $7 < z < 8$ subsample of galaxies, as shown in the top-left panel of Fig. 6.

In Fig. 10, we show the amount of reddening that β may undergo with the introduction of dust attenuation with $E(B-V) = 0.05$, corresponding to $A_V = 0.14$ following the SMC dust attenuation curve (middle panel) and $E(B-V) = 0.10$ corresponding to $A_V = 0.28$ (right panel). We note that in our modelling, the stellar and nebular continuum spectra are affected by dust attenuation in the same manner. Clearly, the observed β-values at $z > 9.5$ require more significant dust attenuation, which was typically seen across our $5.5 < z < 8$ galaxies inferred from the Balmer decrements.

However, the physical arguments behind the importance of the role of dust specifically at $z > 9.5$ are more nuanced. The main challenge with achieving dust attenuation at these early redshifts

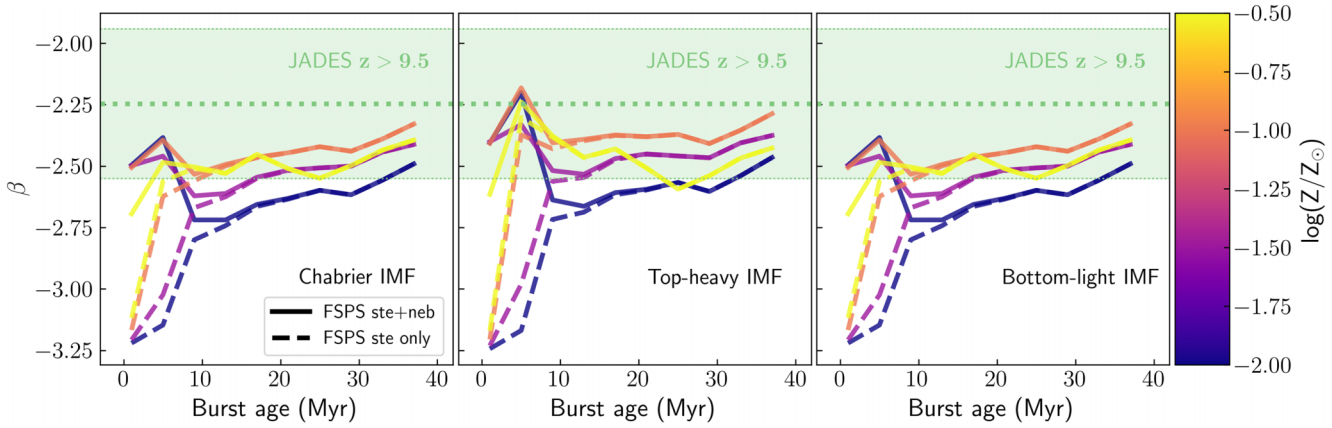

Figure 11. Same as Fig. 9, with the left panel showing predictions using Chabrier IMF, middle panel showing top-heavy IMF, and the right panel showing outputs from a bottom-light IMF. The parametrization of these non-standard IMFs can be found in the text. Qualitatively speaking, there is not much difference between the predictions from Chabrier and bottom-light IMF, but a top-heavy IMF is able to produce redder β-values for younger burst ages, getting closer to the median β measured for our $z > 9.5$ galaxies. Redder β-values are likely driven by the presence of a larger number of hot, massive, but short-lived stars in a top-heavy IMF.

is primarily dependent on rapid dust production through stellar evolution (e.g. R. Valiante et al. 2009; C. Gall, J. Hjorth & A. C. Andersen 2011), growth, and the prevention of dust destruction from intense stellar feedback. Core-collapse supernovae are contemplated to be the most likely sources of dust production at early epochs, due to their short lifetimes and production of metals (e.g. T. Nozawa et al. 2010). Additionally, intermediate- and high-mass AGB stars (with masses between $3 - 8\,M_\odot$) that have sufficiently short lifetimes ($10^7 - 10^8$ yr) may also be potential contributors to dust production (e.g. R. Schneider et al. 2014), although their contribution is highly dependent on the formation time-scales of the first stars in galaxies.

D. Narayanan et al. (2024) recently showed that trace amount of dust attenuation may indeed be reflected in the UV slopes of galaxies at $z > 9.5$, however the fraction of galaxies that show an appreciable dust reddening rapidly plummets at redshifts higher than 9.5. Beyond $z > 10$, dust masses $> 10^6\,M_\odot$ were not seen in the simulations of D. Narayanan et al. (2024), which resulted in minimal dust reddening of the UV slopes. Dust attenuation certainly becomes more pronounced at lower redshifts due to enhanced grain growth per unit dust mass out to redshifts of ~ 6. Therefore, it remains unclear whether dust attenuation represents the dominant reddening mechanism for UV slopes of galaxies particularly at $z > 9.5$. As D. Narayanan et al. (2024) note, nebular continuum can efficiently redden the UV slope by an additional $\Delta\beta = 0.2 - 0.4$, whereas dust attenuation at $z > 9.5$ only leads to $\Delta\beta < 0.1$. Owing to challenges with the rapid production, growth and preservation of dust in very high-redshift galaxies, where it may be easy to destroy and displace dust due to stellar feedback (e.g. A. Ferrara 2024), high dust masses leading to significant reddening of the observed UV slopes might not be feasible.

4.4 The role of the initial mass function

In this section, we explore the role of the IMF in setting the observed UV slopes, in the absence of substantial dust attenuation. In addition to the standard G. Chabrier (2003) IMF with an upper mass cut-off of $150\,M_\odot$ that was employed earlier, we introduce two new IMF prescriptions here. The first 'non-standard' IMF that is the so-called 'top-heavy' IMF, with a lower mass ($M_\star < 0.8\,M_\odot$) slope of -1.3 and a high-mass slope of -1.6 (e.g. J. Dabringhausen, P. Kroupa & H. Baumgardt 2009) with a maximum stellar mass of $600\,M_\odot$, where the slope describes the distribution function $dn \propto m^\gamma\,dm$, where m is the birth mass of the star (e.g. H. Fukushima & H. Yajima 2023). It has been argued that the 'turnover' of the IMF is dependent on the minimum temperature of the molecular clouds out of which stars form, which in turn is linked to the cosmic microwave background temperature, $T_{\rm CMB}$ (e.g. N. Bastian, K. R. Covey & M. R. Meyer 2010). The increasing $T_{\rm CMB}$ at high redshifts will, therefore, result in lesser fragmentation in star-forming clouds, potentially leading to larger number of high-mass stars and a more top-heavy IMF (e.g. R. S. Klessen & S. C. O. Glover 2023).

We additionally include a 'bottom-light' IMF, which instead of boosting the high-mass end of the IMF compared to a standard Chabrier/Salpeter IMF results in suppressing the lower mass end of the IMF. Evidence for a bottom-light IMF in massive star clusters has been recently presented by H. Baumgardt et al. (2023), and we use their parametrization here. For low-mass stars with $M_\star < 0.4\,M_\odot$, the slope is -0.3, for intermediate-mass stars in the mass range $0.4 < M_\star/M_\odot < 1.0$ the slope is -1.65, and for high-mass stars with $M_\star > 1.0\,M_\odot$, the slope of the IMF is -2.3.

In Fig. 11, we show the evolution of β as a function of burst age at $\log(U) = -2.0$, with the standard Chabrier IMF output on the left, the top-heavy IMF in the middle and the bottom-light IMF on the right. It is clear that qualitatively speaking, there is no appreciable difference between the Chabrier and bottom-light IMFs. However, the top-heavy IMF implementation results in overall redder β slopes across all burst ages, even achieving $\beta = -2.2$ that no other model could achieve. The reddest β slopes are once again only obtained via the inclusion of nebular continuum at ages younger than 10 Myr. The effect of metallicity across all IMFs is broadly consistent with one another, with extremely low metallicities capable of producing redder β slopes at low ages with the inclusion of nebular continuum. However at later times, once the fractional contribution of nebular emission is next to negligible, lower metallicities result in bluer β-values.

This exercise demonstrates that a top-heavy IMF does help bring the model-predicted β closer to that which is observed from

galaxies at $z > 9.5$ by significantly boosting the fractional contribution of the nebular continuum to the rest-frame UV spectra. However, although a larger number of hotter, high-mass stars are produced in a top-heavy IMF, they do not live for long enough (R. S. Klessen & S. C. O. Glover 2023) to sufficiently heat up the nebular gas and redden β for longer periods of time after the initial burst. Therefore, to both redden the β as well as maintain a high enough total UV luminosity, inclusion of significant nebular continuum at low burst ages may be preferred explanation (see also H. Katz et al. 2024).

4.5 The role of gas temperature and density on the nebular continuum

Building on the finding that the nebular continuum component may be important to redden the UV slopes of galaxies at $z > 9.5$, in this section we qualitatively explore how the strength and shape of the nebular continuum may vary with changes in the physical properties, particularly the temperature and density, of the nebular gas, which in turn will be driven by stars with different masses and temperatures. *JWST* observations have shown that the ISM density increases dramatically from $z \sim 0$ to ~ 9 (Y. Isobe et al. 2023).

Additionally, it has also been shown that the ionizing photon production rates in galaxies increase steadily towards high redshifts (e.g. C. Simmonds et al. 2024b), although recent evidence from more complete samples has suggested that the evolution with redshift may not be as significant (C. Simmonds et al. 2024a). A higher $\xi_{\rm ion}$ at high redshifts would imply that the underlying stellar populations likely contain hotter, more massive stars that may also be capable of heating up the gas to higher temperatures than those that might be seen at lower redshifts, resulting in a greater fractional contribution from the nebular continuum to the overall UV spectrum (e.g. M. Curti et al. 2023; H. Katz et al. 2023; R. L. Sanders et al. 2023; A. J. Cameron et al. 2023a; I. H. Laseter et al. 2024). Additional heating sources such as high-mass X-ray binaries, which become more important at lower metallicities at high redshifts (e.g. A. Saxena et al. 2021), or even the presence of AGN may further aid in heating the gas to higher temperatures.

H. Katz et al. (2024) recently reported a sample of spectroscopically confirmed star-forming galaxies that show signatures of a nebular-dominated continuum. Using SPS and photoionization models, H. Katz et al. (2024) showed that the fractional contribution of the nebular continuum to the observed rest-UV continuum of galaxies critically depends on stellar temperatures, as well as the temperature and density of the gas. As we previously demonstrated, the IMF can also play a crucial role in boosting the nebular continuum.

To explore how the nebular continuum may change under different physical conditions, in this section, we adopt a simpler approach compared to H. Katz et al. (2024) and create synthetic nebular continuum and line emission spectra using the NEBULAR code[4] (M. Schirmer 2016). NEBULAR allows the synthesis of nebular continuum and line emission from a mixed hydrogen and helium gas in collisional ionization equilibrium. NEBULAR can create spectra over a range of temperatures and densities, and includes contribution from free-free, free-bound, two-photon and line emission from H I, He I, and He II. The goal of this exercise is simply to qualitatively investigate what kinds of physical conditions in the ISM can preferentially redden the observed UV slopes, under the assumption that the observed galaxy spectrum may contain a considerable fraction of nebular continuum emission.

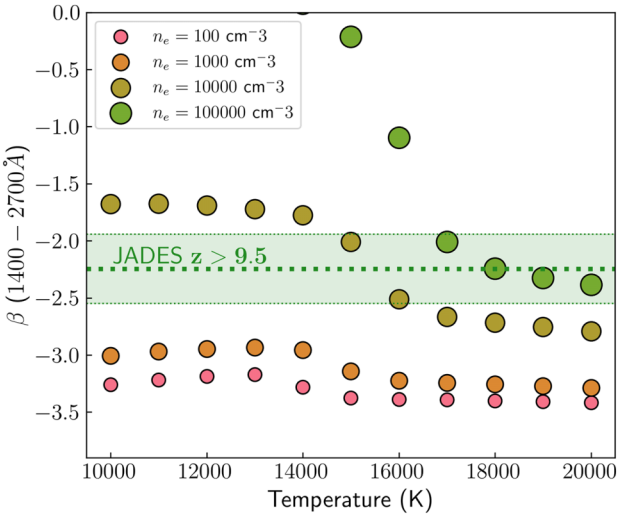

Figure 12. Dependence of β with gas temperature for a purely nebular-dominated rest-frame UV spectrum over the wavelength range where β is typically measured, for a range of electron densities. We find that to reproduce the observed distribution of β-values seen at $z > 9.5$ from our sample in the typically observed density range $n_e = 100 - 1000\,{\rm cm}^{-3}$, a purely nebular-dominated UV continuum from gas at temperatures above 15 000 K is needed. In reality, however, the observed spectrum will contain only a fractional contribution of nebular continuum, but higher temperatures are nonetheless needed to redden the β-values.

In Fig. 12, we show the measured β from synthetic nebular only spectra generated using NEBULAR, over an electron density range of $n_e = [100, 100000]\,{\rm cm}^{-3}$ (in log space) and temperature range $T = [10\,000, 20\,000]$ K. The size of the marker scales with density, with the smallest point having the lowest density and the largest point having the highest density.

The nebular emission from gas below temperatures of $T < 15\,000$ K produces a very blue spectrum for densities $\leq 1000\,{\rm cm}^{-3}$, and no amount of fractional contribution from such nebular emission will significantly redden the observed UV slope of galaxies. For typical densities of $n_e = 100 - 1000\,{\rm cm}^{-3}$ that are measured from spectra of high-redshift galaxies, the nebular continuum emission remains bluer than $\beta < -2.5$, and will therefore be incapable of explaining the range of β-values seen in our $z > 9.5$ spectroscopic sample via a purely nebular dominated UV continuum. At densities $> 1000\,{\rm cm}^{-3}$, a purely nebular continuum dominated spectrum becomes increasingly redder with decreasing temperatures, falling in line with the distribution of β seen in our $z > 9.5$ sample. Even higher densities are capable of reddening the continuum spectra further, as higher densities significantly boost the free–bound and free–free contribution to the nebular continuum.

We note here that over the wavelength range that is used to measure the UV slope, the two-photon component does not have an appreciable impact. As also discussed by A. J. Cameron et al. (2023b), the two-photon component of the nebular continuum is more prominent at lower electron densities ($n_e < 1000\,{\rm cm}^{-3}$),

[4] https://github.com/mischaschirmer/nebular/

but at higher densities the reddening of β is likely caused by the free–bound component.

4.6 Implications for the observed galaxy properties at $z > 9.5$

Thus far we have demonstrated that the UV slopes of spectroscopically confirmed galaxies at $z > 9.5$ appear to redden, deviating from the trend of bluer β observed with increasing redshift observed at $z < 9.5$. We have also shown that to explain these relatively redder UV slopes in some of the highest redshift galaxies, inclusion of nebular continuum emission and/or dust attenuation may be required, particularly when stars forming out of relatively metal-free gas would be expected to be more massive and hotter, with the stellar emission peaking at even shorter wavelengths, leading to a blue β from starlight alone. Trace amounts of dust ($A_V \sim 0.2 - 0.3$) may be able to explain the observed distribution of β at $z > 9.5$, but producing and growing enough dust at these early epochs is challenging from a modelling perspective (see D. Narayanan et al. 2024, for example).

Furthermore, we have shown that with increasing gas densities ($> 10\,000\,\mathrm{cm}^{-3}$), the nebular continuum emission has redder UV slopes. We find that pure nebular continuum emission from gas at densities lower than $1000\,\mathrm{cm}^{-3}$ produces a much bluer continuum slope (measured between rest-frame $1400 - 2700\,\text{Å}$) than what is seen across our $z > 9.5$ sample across a range of gas temperatures. This suggests that, in the absence of appreciable amounts of dust, bright nebular continuum from dense gas can redden the observed UV slopes of galaxies, particularly when the fractional contribution of the nebular continuum is high. A handful of examples of nebular dominated galaxy UV spectra across redshifts have been previously reported in the literature (e.g. R. A. E. Fosbury et al. 2003; A. J. Cameron et al. 2023a; H. Katz et al. 2024; L. Mowla et al. 2024), where little to no stellar emission is needed to explain the observed UV continuum, and a careful analysis of the inferred gas densities in these systems may shed light on the role of nebular continuum in reddening the observed UV slope.

Naturally an increased fractional contribution of nebular emission to the continuum light of a galaxy will have implications on the inferred galaxy properties from observations. We begin our discussion by tackling the question of the extremely bright absolute UV magnitudes that have been observed at record distances, particularly in sources such as GN-z11 (A. J. Bunker et al. 2023b) that have been shown to have a high gas density (R. Maiolino et al. 2024), GS-z12 (F. D'Eugenio et al. 2023) and GS-z14-0 (S. Carniani et al. 2024) in our sample, as well as GHZ2 (M. Castellano et al. 2024). Interestingly, all of these galaxies show relatively red β slopes (-2.0 to -2.5). A further overabundance of photometrically selected UV-bright galaxies at $z > 10$ has also been reported widely (e.g. B. Robertson et al. 2023; N. J. Adams et al. 2024; I. Chemerynska et al. 2024; C. T. Donnan et al. 2024; D. J. McLeod et al. 2024). If the UV continuum of these galaxies does contain a higher fraction of nebular emission (e.g. H. Katz et al. 2024), then the observed UV magnitudes will be brighter without the need to boost the underlying stellar masses via extremely high star formation efficiencies (e.g. K. Inayoshi et al. 2022; A. Dekel et al. 2023). Such a scenario may explain both the extremely bright UV magnitudes of a large number of $z > 10$ galaxies, as well as their relatively redder UV slopes.

With the exception of GN-z11, GS-z12, and GHZ2, the vast majority of spectroscopically confirmed galaxies at $z > 10$ do not show strong rest-frame UV emission lines in their spectra (e.g. S. L. Finkelstein et al. 2022; P. Arrabal Haro et al. 2023; E. Curtis-Lake et al. 2023; S. Carniani et al. 2024; K. N. Hainline et al. 2024). If the UV continuum is boosted by nebular emission at higher gas densities, then this may play a role in lowering the observed EWs of the rest-frame UV emission lines, making them harder to detect even with deep *JWST* spectroscopy. Other plausible explanations for the non-detection of emission lines in the vast majority of galaxies are either extremely low metallicities or high LyC escape fractions. A high LyC escape fraction will make the UV slope of the galaxies bluer than what is typically observed by suppressing the contribution of both the nebular continuum and line emission from the spectrum (e.g. E. Zackrisson, A. K. Inoue & H. Jensen 2013). Lower metallicities may therefore be preferable as an explanation, which as we showed in Fig. 9 will also self consistently lead to redder β-values at lower burst ages.

We showed that by increasing the gas densities in the ISM, which can theoretically be probed by observing commonly observed doublet line ratios, overall redder UV slopes from nebular continuum emission can be achieved. Several large sample studies across low and intermediate redshifts (out to $z \sim 4$) have shown that the gas in star-forming regions becomes more dense with increasing redshift, which holds both for warm ionized gas (e.g. M. Shirazi, J. Brinchmann & A. Rahmati 2014) and cold molecular gas (e.g. M. Rybak et al. 2026). Therefore, a significant increase in the density of gas that fuels star formation and forms the nebular emission region at extremely high redshifts could offer a natural explanation to the increasingly redder UV slopes at $z > 9.5$ reported in this study.

Finally, we also note again that for our $z < 9.5$ sample, based on the relationship between O32 and β we inferred that more complicated ISM geometries may need to be considered (e.g. Y. Jin et al. 2022; H. Katz et al. 2022) or prevalence of ionization-bounded H II regions may be needed to explain the decrease in O32 ratios at the bluest UV slopes. These scenarios become important when the galaxies are undergoing periods of intense star formation that introduces turbulence in the ISM. Galaxies at $z > 9.5$, owing to their youthfulness, will likely also experience highly turbulent ISM conditions, and it remains unclear what impact these effects have on the ISM of $z > 9.5$ galaxies, and what it means for the predicted nebular continuum emission and effect on observed UV slopes.

5 SUMMARY

In this study, we have presented spectroscopic measurements of the rest-frame UV slope, β, for a sample of 395 galaxies at $z > 5$ using *JWST*/NIRSpec observations, using both individual measurements as well as measurements from stacked spectra created in bins of redshift and β. All our galaxies have robust spectroscopic redshifts, which enables a highly reliable estimate of β for our sample. The main aims of this study are to characterize which physical and chemical conditions are responsible for setting the observed β in high-redshift galaxies, and what the global evolution of β as a function of galaxy properties and redshifts can tell us about the evolving properties of galaxies over cosmic time.

Across our sample, we find a median β-value of -2.15 and a mild increase in the blueness of β with redshift. On the other hand, we find evidence of increased reddening of β at $z > 9.5$ compared to its evolution at lower redshifts. We further find a weak trend of increasingly bluer β at fainter absolute UV magnitudes. This trend between β and UV magnitude is found to be

stronger at $z < 7$, with the trend breaking down at $z > 7$. Overall we find that the range of β-values remains large and consistent across redshifts.

Based on spectroscopic measurements performed on spectra stacked in bins of β and redshift, we find that galaxies with the bluest β generally have little to no dust inferred from the Balmer decrements, with nearly all galaxies above $z > 8$ exhibiting $E(B-V) < 0.2$ regardless of their β slope. The UV slope does not show any clear trend with gas-phase metallicities. When comparing the [O III] λ5007/[O II] λ3727 (O32) ratios, we find that galaxies with bluer β generally show higher O32 ratios. However, for galaxies between redshifts of $8 < z < 9.5$, we find that the O32 ratio decreases for the bin with the bluest β ($\beta \approx -2.6$) compared to what is seen for the intermediate β bin ($\beta \approx -2.2$). Finally, we generally see increasing strength of the Balmer emission lines with increasingly blue β.

From our sample, we identify five galaxies that have ultra-blue $\beta < -2.9$, which all show interesting spectroscopic features. These galaxies span a redshift range of $z = 5.5$ to 13.2, and two out of the five galaxies show strong Lyα emission. In general, the galaxies have extremely high values of the ionization photon production efficiency parameter, $\xi_{\rm ion}$, and exhibit traits expected from LyC photon leakers.

We then explore β-values in our $z > 9.5$ galaxy subsample, finding a median $\beta = -2.3$, with 1σ dispersion ranging from $\beta - 2.0$ to -2.6. When comparing with SSP models, we find that models that only take into account emission from young, metal-poor stars produce β slopes that are too blue when compared with the observed values. Therefore, inclusion of nebular continuum is necessary to get closer to explaining the observed β-values at $z > 9.5$, but some of the reddest observed β-values still remain out of reach of these models. We show that inclusion of a trace amount of dust attenuation can help redden the model β slopes. Furthermore, in the absence of dust attenuation, using a more top-heavy IMF also results in overall redder UV slopes.

Focusing on the role of the nebular continuum in reddening the UV slopes, we then show that increasing the gas densities above 10 000 cm^{-3} produces red β-values over a large range of gas temperatures. For typical densities of $n_e = 100 - 1000\,{\rm cm}^{-3}$,the nebular continuum emission remains bluer than $\beta < -2.5$. Accurate measurements of the evolution of the (multiphase) gas density at increasingly higher redshifts may hold they key that could explain the reddening of the observed UV slopes at $z > 9.5$ in the absence of significant amounts of dust.

In this work, we have demonstrated that a purely spectroscopic analysis of the UV slope of a large sample of galaxies at $z > 5$ is now possible thanks to a number of large spectroscopic surveys that *JWST* has been carrying out over the last few years. Establishing the conditions that drive the all-important rest-UV slope of galaxies in the presence of valuable spectroscopic information for galaxies at the highest redshifts is a remarkable step forward for high-redshift galaxy evolution studies, and more detailed modelling may be needed to understand the spectroscopic and photometric properties of some of the earliest galaxies that formed in the Universe.

ACKNOWLEDGEMENTS

We thank the anonymous referee for a detailed and constructive report than helped improve the quality of this manuscript. AS would like to thank Nick Choustikov for useful discussions about LyC leakage from galaxies with blue UV slopes. AS thanks Richard Ellis for fruitful discussions. AS, AJC, AJB, and JC acknowledge funding from the 'FirstGalaxies' Advanced Grant from the European Research Council (ERC) under the European Union's Horizon 2020 research and innovation programme (grant agreement no. 789056). FDE, GCJ, CS, and ST acknowledge support by the Science and Technology Facilities Council (STFC) and by the ERC through Advanced grant no. 695671 'QUENCH', and by the UKRI Frontier Research grant RISE-andFALL. SA acknowledges support from the research project PID2021-127718NB- I00 of the Spanish Ministry of Science and Innovation/State Agency of Research (MICIN/AEI). SC acknowledges support by European Union's HE ERC Starting grant no. 101040227 – 'WINGS'. ECL acknowledges support of an STFC Webb Fellowship (ST/W001438/1). BDJ and BER acknowledge support from the NIRCam Science Team contract to the University of Arizona, NAS5-02015. HÜ acknowledges support through the ERC Starting grant 101164796 'APEX'. The work of CCW is supported by NOIR-Lab, which is managed by the Association of Universities for Research in Astronomy (AURA) under a cooperative agreement with the National Science Foundation.

This work is based on observations made with the NASA/ESA/CSA *James Webb Space Telescope*. The data were obtained from the Mikulski Archive for Space Telescopes at the Space Telescope Science Institute, which is operated by the Association of Universities for Research in Astronomy, Inc., under NASA contract NAS 5–03127 for *JWST*. These observations are associated with programme nos 1180, 1181, 1210, 1286, 1287, and 3215.

This work has made extensive use of the ASTROPY (Astropy Collaboration 2013, 2018), MATPLOTLIB (J. D. Hunter 2007), and PANDAS (T. team 2020) PYTHON packages. This work would not have been possible without the hard work of thousands of developers and volunteers around the world, who foster a culture of open source software development.

DATA AVAILABILITY

The high-level science products (HLSP) underlying this analysis are either available in full or in part both from the JADES collaboration webpage (https://jades-survey.github.io) and from the Mikulski Archive for Space Telescope (https://archive.stsci.edu/hlsp/jades). The data analysis pipelines used in this paper will shortly be made available on the lead author's GitHub page (https://github.com/aayush3009), and are immediately available upon reasonable request.

REFERENCES

Adams N. J. et al., 2024, ApJ, 965, 169
Arrabal Haro P. et al., 2023, ApJ, 951, L22
Astropy Collaboration, 2013, A&A, 558, A33
Astropy Collaboration, 2018, AJ, 156, 123
Austin D. et al., 2025, ApJ, 995, 43
Bastian N., Covey K. R., Meyer M. R., 2010, ARA&A, 48, 339
Baumgardt H., Hénault-Brunet V., Dickson N., Sollima A., 2023, MNRAS, 521, 3991
Bhatawdekar R., Conselice C. J., 2021, ApJ, 909, 144
Bolamperti A. et al., 2023, MNRAS, 526, 5263
Bouwens R., Illingworth G., Oesch P., Stefanon M., Naidu R., van Leeuwen I., Magee D., 2023, MNRAS, 523, 1009
Bouwens R. J. et al., 2009, ApJ, 705, 936
Bouwens R. J. et al., 2010, ApJ, 708, L69
Bouwens R. J. et al., 2014, ApJ, 793, 115

Bouwens R. J. et al., 2023, MNRAS, 523, 1036
Bunker A. J., NIRSPEC Instrument Science Team, , in JAESs Collaboration,, in 2020, in da Cunha E., Hodge J., Afonso J., Pentericci L., Sobral D. eds, IAU Symp. Vol. 352, Uncovering Early Galaxy Evolution in the ALMA and JWST Era, p. 342, preprint (arXiv:2112.15207)
Bunker A. J. et al., 2023a, preprint (arXiv:2306.02467)
Bunker A. J. et al., 2023b, A&A, 677, A88
Byler N., Dalcanton J. J., Conroy C., Johnson B. D., 2017, ApJ, 840, 44
Calabrò A. et al., 2021, A&A, 646, A39
Calzetti D., Kinney A. L., Storchi-Bergmann T., 1994, ApJ, 429, 582
Cameron A. J., Katz H., Witten C., Saxena A., Laporte N., Bunker A. J., 2023a, preprint (arXiv:2311.02051)
Cameron A. J., Katz H., Rey M. P., 2023b, MNRAS, 522, L89
Carnall A. C., McLure R. J., Dunlop J. S., Davé R., 2018, MNRAS, 480, 4379
Carniani S. et al., 2024, preprint (arXiv:2405.18485)
Carreira C. et al., 2026, preprint (arXiv:2601.15957)
Castellano M. et al., 2024, preprint (arXiv:2403.10238)
Chabrier G., 2003, PASP, 115, 763
Chemerynska I. et al., 2024, MNRAS, 531, 2615
Chisholm J. et al., 2022, MNRAS, 517, 5104
Choi J., Dotter A., Conroy C., Cantiello M., Paxton B., Johnson B. D., 2016, ApJ, 823, 102
Choustikov N. et al., 2024a, MNRAS, 529, 3751
Choustikov N. et al., 2024b, MNRAS, 532, 2463
Conroy C., Gunn J. E., 2010, ApJ, 712, 833
Conroy C., Gunn J. E., White M., 2009, ApJ, 699, 486
Cullen F. et al., 2021, MNRAS, 505, 903
Cullen F. et al., 2023a, MNRAS 520, 14
Cullen F. et al., 2023b, preprint (arXiv:2311.06209)
Curti M., Mannucci F., Cresci G., Maiolino R., 2020, MNRAS, 491, 944
Curti M. et al., 2023, MNRAS, 518, 425
Curtis-Lake E. et al., 2023, Nat. Astron., 7, 622
D'Eugenio F. et al., 2023, preprint (arXiv:2311.09908)
D'Eugenio F. et al., 2024, preprint (arXiv:2404.06531)
Dabringhausen J., Kroupa P., Baumgardt H., 2009, MNRAS, 394, 1529
Dekel A., Sarkar K. C., Birnboim Y., Mandelker N., Li Z., 2023, MNRAS, 523, 3201
Donnan C. T. et al., 2024, preprint (arXiv:2403.03171)
Dotter A., 2016, ApJS, 222, 8
Dunlop J. S., McLure R. J., Robertson B. E., Ellis R. S., Stark D. P., Cirasuolo M., de Ravel L., 2012, MNRAS, 420, 901
Eisenstein D. J. et al., 2023a, preprint (arXiv:2306.02465)
Eisenstein D. J. et al., 2023b, preprint (arXiv:2310.12340)
Eldridge J. J., Stanway E. R., Xiao L., McClelland L. A. S., Taylor G., Ng M., Greis S. M. L., Bray J. C., 2017, Publ. Astron. Soc. Aust., 34, e058
Endsley R., Stark D. P., Whitler L., Topping M. W., Chen Z., Plat A., Chisholm J., Charlot S., 2023, MNRAS, 524, 2312
Falcón-Barroso J., Sánchez-Blázquez P., Vazdekis A., Ricciardelli E., Cardiel N., Cenarro A. J., Gorgas J., Peletier R. F., 2011, A&A, 532, A95
Faucher-Giguère C.-A., 2018, MNRAS, 473, 3717
Ferrara A., 2024, preprint (arXiv:2405.20370)
Ferruit P. et al., 2022, A&A, 661, A81
Finkelstein S. L., Papovich C., Giavalisco M., Reddy N. A., Ferguson H. C., Koekemoer A. M., Dickinson M., 2010, ApJ, 719, 1250
Finkelstein S. L. et al., 2012, ApJ, 756, 164
Finkelstein S. L. et al., 2022, ApJ, 940, L55
Flury S. R. et al., 2022, ApJ, 930, 126
Fosbury R. A. E. et al., 2003, ApJ, 596, 797
Fukushima H., Yajima H., 2023, MNRAS, 524, 1422
Furlanetto S. R., Mirocha J., 2022, MNRAS, 511, 3895
Furtak L. J., Shuntov M., Atek H., Zitrin A., Richard J., Lehnert M. D., Chevallard J., 2023, MNRAS, 519, 3064
Gall C., Hjorth J., Andersen A. C., 2011, A&AR, 19, 43
Hägele G. F., Pérez-Montero E., Díaz Á. I., Terlevich E., Terlevich R., 2006, MNRAS, 372, 293
Hainline K. N. et al., 2024, preprint (arXiv:2404.04325)
Hayes M. J., Saldana-Lopez A., Citro A., James B. L., Mingozzi M., Scarlata C., Martinez Z., Berg D. A., 2024, preprint (arXiv:2411.09262)
Heintz K. E. et al., 2024, preprint (arXiv:2404.02211)
Hunter J. D., 2007, Comput. Sci. Eng., 9, 90
Inayoshi K., Harikane Y., Inoue A. K., Li W., Ho L. C., 2022, ApJ, 938, L10
Isobe Y., Ouchi M., Nakajima K., Harikane Y., Ono Y., Xu Y., Zhang Y., Umeda H., 2023, ApJ, 956, 139
Jakobsen P. et al., 2022, A&A, 661, A80
Jaskot A. E., Oey M. S., 2013, ApJ, 766, 91
Jaskot A. E. et al., 2024, ApJ, 973, 111
Jin Y., Kewley L. J., Sutherland R. S., 2022, ApJ, 934, L8
Johnson B. et al., 2024, dfm/python-fsps: v0.4.7, Zenodo, https://doi.org/10.5281/zenodo.12447779
Katz H. et al., 2022, preprint (arXiv:2211.04626)
Katz H. et al., 2023, MNRAS, 518, 592
Katz H. et al., 2024, preprint (arXiv:2408.03189)
Klessen R. S., Glover S. C. O., 2023, ARA&A, 61, 65
Laseter I. H. et al., 2024, A&A, 681, A70
Lecroq M. et al., 2024, MNRAS, 527, 9480
Leitherer C., 2005, in Hüttmeister S., Manthey E., Bomans D., Weis K. eds, AIP Conf. Ser. Vol. 783, The Evolution of Starbursts. AIP, p. 280, preprint (astro-ph/0409407)
Levesque E. M., Leitherer C., 2013, ApJ, 779, 170
Looser T. J. et al., 2024, Nature, 629, 53
Looser T. J. et al., 2025, A&A, 697, A88
Luridiana V., Morisset C., Shaw R. A., 2015, A&A, 573, A42
Lyu J. et al., 2024, ApJ, 966, 229
Maiolino R. et al., 2023, preprint (arXiv:2308.01230)
Maiolino R. et al., 2024, Nature, 627, 59
Mascia S. et al., 2023, A&A, 672, A155
McClymont W. et al., 2024, preprint (arXiv:2405.15859)
McClymont W. et al., 2025, MNRAS, 544, 513
McLeod D. J. et al., 2024, MNRAS, 527, 5004
McLure R. J. et al., 2011, MNRAS, 418, 2074
Meyer R. A. et al., 2024, preprint (arXiv:2405.05111)
Mirocha J., Furlanetto S. R., 2023, MNRAS, 519, 843
Mowla L. et al., 2024, preprint (arXiv:2402.08696)
Nakajima K., Ouchi M., Isobe Y., Harikane Y., Zhang Y., Ono Y., Umeda H., Oguri M., 2023, ApJS, 269, 33
Nanayakkara T. et al., 2023, ApJ, 947, L26
Narayanan D. et al., 2024, preprint (arXiv:2408.13312)
Nozawa T., Kozasa T., Tominaga N., Maeda K., Umeda H., Nomoto K., Krause O., 2010, ApJ, 713, 356
Oke J. B., Gunn J. E., 1983, ApJ, 266, 713
Ormerod K. et al., 2024, MNRAS, 527, 6110
Osterbrock D. E., Ferland G. J., 2006, Astrophysics of Gaseous Nebulae and Active Galactic Nuclei
Paalvast M. et al., 2018, A&A, 618, A40
pandas development team T., 2020, pandas-dev/pandas: Pandas, Zenodo, https://doi.org/10.5281/zenodo.3509134
Pérez-Montero E., 2017, PASP, 129, 043001
Planck Collaboration VI, 2020, A&A, 641, A6
Raiter A., Schaerer D., Fosbury R. A. E., 2010, A&A, 523, A64
Rieke M. J. et al., 2023, ApJS, 269, 16
Roberts-Borsani G. et al., 2024, preprint (arXiv:2403.07103)
Robertson B. et al., 2023, preprint (arXiv:2312.10033)
Robertson B. E. et al., 2026, preprint (arXiv:2601.15956)
Rybak M. et al., 2026, A&A, 706, A69
Sánchez-Blázquez P. et al., 2006, MNRAS, 371, 703
Sanders R. L., Shapley A. E., Topping M. W., Reddy N. A., Brammer G. B., 2023, ApJ, 955, 54
Saxena A. et al., 2020, A&A, 636, A47
Saxena A. et al., 2021, MNRAS, 505, 4798
Saxena A. et al., 2023, A&A, 678, A68
Saxena A. et al., 2024, A&A, 684, A84
Scarlata C., Hayes M., Panagia N., Mehta V., Haardt F., Bagley M., 2024, preprint (arXiv:2404.09015)

Schaerer D., Pelló R., 2005, MNRAS, 362, 1054
Schirmer M., 2016, PASP, 128, 114001
Schneider R., Valiante R., Ventura P., dell'Agli F., Di Criscienzo M., Hirashita H., Kemper F., 2014, MNRAS, 442, 1440
Scholtz J. et al., 2023, preprint (arXiv:2311.18731)
Shirazi M., Brinchmann J., Rahmati A., 2014, ApJ, 787, 120
Simmonds C. et al., 2024a, preprint (arXiv:2409.01286)
Simmonds C. et al., 2024b, MNRAS, 527, 6139
Sun G., Faucher-Giguère C.-A., Hayward C. C., Shen X., 2023, MNRAS, 526, 2665
Tacchella S., Forbes J. C., Caplar N., 2020, MNRAS, 497, 698
Tacchella S. et al., 2022, ApJ, 927, 170
Topping M. W., Stark D. P., Endsley R., Plat A., Whitler L., Chen Z., Charlot S., 2022, ApJ, 941, 153
Topping M. W. et al., 2024, MNRAS, 529, 4087
Trussler J. A. A. et al., 2025, MNRAS, 537, 3662
Valiante R., Schneider R., Bianchi S., Andersen A. C., 2009, MNRAS, 397, 1661
Verhamme A., Orlitová I., Schaerer D., Hayes M., 2015, A&A, 578, A7
Wilkins S. M., Bunker A., Coulton W., Croft R., di Matteo T., Khandai N., Feng Y., 2013, MNRAS, 430, 2885
Witstok J. et al., 2023, preprint (arXiv:2306.04627)
Witstok J. et al., 2024, preprint (arXiv:2404.05724)
Witten C. et al., 2025, MNRAS, 537, 112
Yanagisawa H. et al., 2024, preprint (arXiv:2403.20118)
Zackrisson E., Inoue A. K., Jensen H., 2013, ApJ, 777, 39

APPENDIX A: STACKED 1D REST-FRAME SPECTRA OF GALAXIES IN REDSHIFT-β BINS

Here, we show the stacked rest-frame spectra in bins of redshift and β, as described in Table 3. The fluxes are normalized in units of F_ν. The stacked spectra are represented by the solid green lines in each bin, with the individual (normalized) spectra going in to the stack shown as translucent grey lines in the background. Also marked are the positions of strong/common emission-line features.

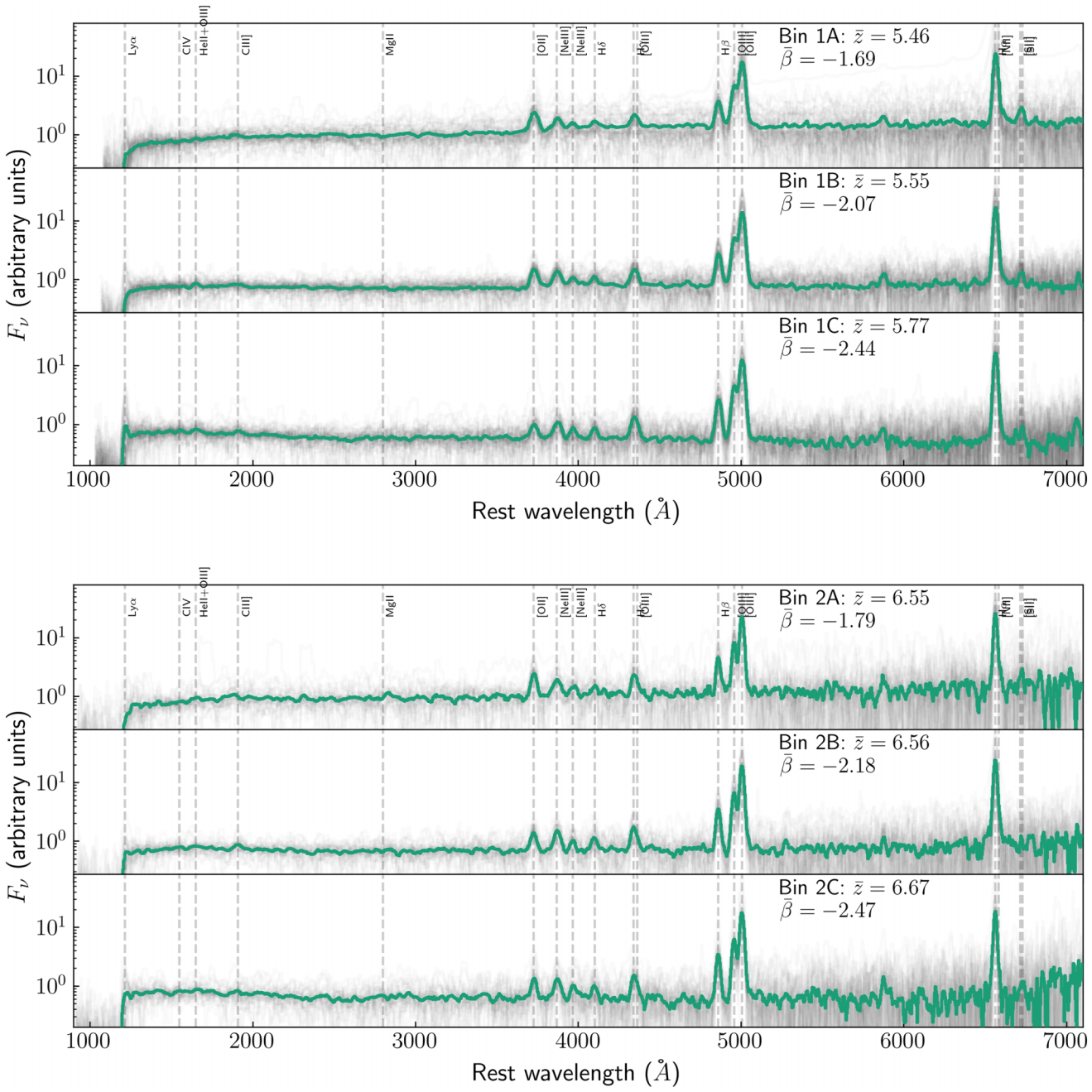

Figure A1. Stacked and normalized rest-frame spectra (in units of F_ν) created in bins of redshift and β (green), with individual spectra that go into the stack shown in grey in the background, as described in Section 2 and in Table 3. The locations of key emission lines have been marked with dashed lines. Each bin shows the median redshift and the β-value measured from the stacked spectrum, which is consistent with the median β in the bin.

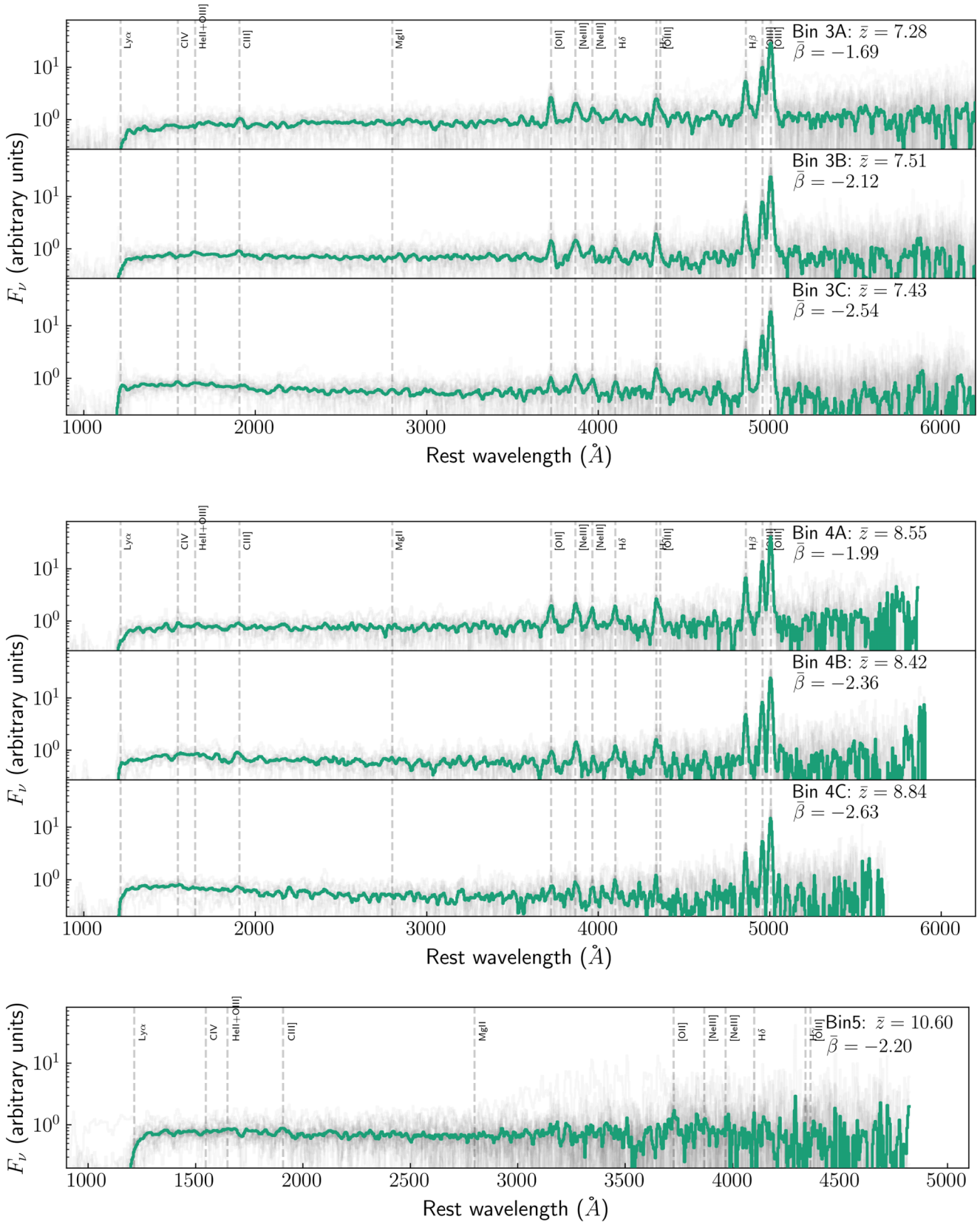

Figure A1. continued.

[1]*Department of Physics, University of Oxford, Denys Wilkinson Building, Keble Road, Oxford OX1 3RH, UK*
[2]*Department of Physics and Astronomy, University College London, Gower Street, London WC1E 6BT, UK*
[3]*Department of Astronomy & Astrophysics, University of Chicago, 5640 S Ellis Avenue, Chicago, IL 60637, USA*
[4]*Kavli Institute for Cosmological Physics, University of Chicago, Chicago IL 60637, USA*
[5]*Kavli Institute for Cosmology, University of Cambridge, Madingley Road, Cambridge CB3 0HA, UK*
[6]*Cavendish Laboratory, University of Cambridge, 19 JJ Thomson Avenue, Cambridge CB3 0HE, UK*
[7]*Centro de Astrobiología (CAB), CSIC–INTA, Cra. de Ajalvir Km. 4, E-28850-Torrejón de Ardoz, Madrid, Spain*
[8]*European Space Agency (ESA), European Space Astronomy Centre (ESAC), Camino Bajo del Castillo s/n, E-28692 Villanueva de la Cañada, Madrid, Spain*
[9]*Center for Astrophysics | Harvard & Smithsonian, 60 Garden St., Cambridge, MA 02138,USA*
[10]*Scuola Normale Superiore, Piazza dei Cavalieri 7, I-56126 Pisa, Italy*
[11]*Sorbonne Université, CNRS, UMR 7095, Institut d'Astrophysique de Paris, 98 bis bd Arago, F-75014 Paris, France*
[12]*European Southern Observatory, Karl-Schwarzschild-Strasse 2, D-85748 Garching, Germany*
[13]*Centre for Astrophysics Research, Department of Physics, Astronomy and Mathematics, University of Hertfordshire, Hatfield AL10 9AB, UK*
[14]*Steward Observatory, University of Arizona, 933 N. Cherry Avenue, Tucson, AZ 85721, USA*
[15]*AURA for European Space Agency, Space Telescope Science Institute, 3700 San Martin Drive. Baltimore, MD 21210*
[16]*Department of Astronomy, University of Wisconsin-Madison, 475 N. Charter St., Madison, WI 53706, USA*
[17]*Department of Astronomy and Astrophysics University of California, Santa Cruz, 1156 High Street, Santa Cruz, CA 96054, USA*
[18]*Max-Planck-Institut für Extraterrestrische Physik (MPE), Gießenbachstraße 1, D-85748 Garching, Germany*
[19]*NSF National Optical-Infrared Astronomy Research Laboratory, 950 North Cherry Avenue, Tucson, AZ 85719, USA*
[20]*NRC Herzberg, 5071 West Saanich Rd, Victoria, BC V9E 2E7, Canada*
[21]*Cosmic Dawn Center (DAWN), Copenhagen, Denmark*
[22]*Niels Bohr Institute, University of Copenhagen, Jagtvej 128, DK-2200, Copenhagen, Denmark*

This paper has been typeset from a TEX/LATEX file prepared by the author.